The Astrophysical Journal, 955:129 (17pp), 2023 October 1 https://doi.org/10.3847/1538-4357/acec4d

High-resolution Chemical Abundances of the Nyx Stream

Shuyu Wang (汪书玉)[1,2], Lina Necib[3,4], Alexander P. Ji[1,2], Xiaowei Ou[5], Mariangela Lisanti[6,7], Mithi A. C. de los Reyes[8,9], Allison L. Strom[10], and Mimi Truong[11]
[1] Department of Astronomy & Astrophysics, University of Chicago, 5640 S Ellis Avenue, Chicago, IL 60637, USA; shuyuwang.astro@gmail.com
[2] Kavli Institute for Cosmological Physics, University of Chicago, Chicago, IL 60637, USA
[3] Department of Physics and Kavli Institute for Astrophysics and Space Research, Massachusetts Institute of Technology, 77 Massachusetts Avenue, Cambridge MA 02139, USA
[4] The NSF AI Institute for Artificial Intelligence and Fundamental Interactions, 77 Massachusetts Avenue, Cambridge MA 02139, USA
[5] Kavli Institute for Astrophysics and Space Research, Massachusetts Institute of Technology, 77 Massachusetts Avenue, Cambridge MA 02139, USA
[6] Department of Physics, Princeton University, Princeton, NJ 08544, USA
[7] Center for Computational Astrophysics, Flatiron Institute, 162 Fifth Avenue, New York, NY 10010, USA
[8] Department of Physics, Stanford University, 382 Via Pueblo Mall, Stanford, CA 94305, USA
[9] Kavli Institute for Particle Astrophysics & Cosmology, P.O. Box 2450, Stanford University, Stanford, CA 94305, USA
[10] Department of Physics and Astronomy and Center for Interdisciplinary Exploration and Research in Astrophysics (CIERA), Northwestern University, 2145 Sheridan Road, Evanston, IL 60208, USA
[11] California State University, Northridge 18111 Nordhoff Street, Northridge, CA 91330, USA
Received 2022 October 26; revised 2023 July 27; accepted 2023 July 29; published 2023 September 26

Abstract

Nyx is a nearby, prograde, and high-eccentricity stellar stream physically contained in the thick disk, but its origin is unknown. Nyx could be the remnant of a disrupted dwarf galaxy, in which case the associated dark matter substructure could affect terrestrial dark matter direct-detection experiments. Alternatively, Nyx could be a signature of the Milky Way's disk formation and evolution. To determine the origin of Nyx, we obtained high-resolution spectroscopy of 34 Nyx stars using Keck/HIRES and Magellan/MIKE. A differential chemical abundance analysis shows that most Nyx stars reside in a metal-rich ([Fe/H] > -1) high-α component that is chemically indistinguishable from the thick disk. This rules out the originally suggested scenario that Nyx is the remnant of a single massive dwarf galaxy merger. However, we also identify 5 substantially more metal-poor stars ([Fe/H] ~ -2.0) whose chemical abundances are similar to those of the metal-weak thick disk. It remains unclear how stars that are chemically identical to the thick disk can be on such prograde, high-eccentricity orbits. We suggest two most likely scenarios: that Nyx is the result of an early minor dwarf galaxy merger, or that it is a record of the early spin-up of the Milky Way disk—although neither perfectly reproduces the chemodynamic observations. The most likely formation scenarios suggest that future spectroscopic surveys should find Nyx-like structures outside of the solar neighborhood.

Unified Astronomy Thesaurus concepts: Stellar abundances (1577); Stellar kinematics (1608); Milky Way formation (1053); Dark matter (353)

Supporting material: machine-readable tables

1. Introduction

The standard Λ cold dark matter paradigm predicts that galaxies form hierarchically (e.g., White & Rees 1978), such that massive galaxies such as the Milky Way grow through the accretion of smaller galaxies. As the Milky Way accretes smaller satellite galaxies, its gravitational potential tidally disrupts these satellites, which can leave behind streams of stars (e.g., Johnston 1998) as well as dark matter (e.g., Read et al. 2008; Herzog-Arbeitman et al. 2018a, 2018b) in the Galaxy. The stellar component of the streams is crucial in understanding the formation of the Milky Way. The dark matter component, or the dark matter substructure, could affect the dark matter phase-space distribution, and thus could have profound implications for the terrestrial direct detection of dark matter. Stream stars retain key information of the chemical abundances and kinematics of their progenitor galaxies long after the accretion events (e.g., McWilliam 1997; Helmi & White 1999; Freeman & Bland-Hawthorn 2002; Venn et al. 2004; Bullock & Johnston 2005; Robertson et al. 2005; Font et al. 2006; Helmi 2008, 2020). Hence, detailed chemodynamic analyses of stars in the tidal debris can be used to identify the origin of a stellar stream and to reconstruct the merger event with the Milky Way, and they might be used to determine the presence of a dark matter substructure accompanying such a merger within the Galaxy.

The advent of all-sky measurements of stellar proper motions from Gaia (Gaia Collaboration et al. 2016a, 2016b, 2018a, 2021) has resulted in the discovery of numerous new kinematic structures in the Milky Way (e.g., Helmi 2020; Naidu et al. 2020; Yuan et al. 2020). These Galactic building blocks include the debris flow referred to as the Gaia-Sausage Enceladus (GSE; Belokurov et al. 2018; Haywood et al. 2018; Helmi et al. 2018; Mackereth et al. 2018), as well as streams such as the Helmi (Helmi & White 1999), Sequoia (Myeong et al. 2019), and Thamnos streams (Koppelman et al. 2019).

One of the most recent discoveries is Nyx, a prograde stellar stream in the solar vicinity (Necib et al. 2020b). Nyx was found after applying clustering algorithms to a catalog of likely

accreted stars from the second data release (DR2) of Gaia (Ostdiek et al. 2020). To build this catalog, Ostdiek et al. (2020) trained a neural network on both a simulation and data using stellar 5D kinematics to distinguish between an accreted or in situ origin. First, the network was trained on the synthetic Gaia catalog `Ananke` (Sanderson et al. 2020), based on Milky Way-like galaxies from the `Latte` suite of simulations (Wetzel et al. 2016), which uses the code called feedback in realistic environments (FIRE) for the hydrodynamic implementation (Hopkins et al. 2014; Hopkins 2015; Hopkins et al. 2018). Then, transfer-learning (Caruana 1994; Bengio 2012) was performed using the RAVE DR5-Gaia DR2 cross match (Kunder et al. 2017). At the end of the training, each Gaia DR2 star received a score $S \in [0, 1]$, where 1 (0) means that the star is likely accreted (in situ). In the resulting accreted catalog, Necib et al. (2020a) rediscovered several known stellar substructures near the Sun in addition to Nyx. The latter stands out as an overdensity of stars confined within 3 kpc of the disk plane that are on prograde orbits, but with high radial velocities (i.e., high eccentricities). The Nyx stream has since been identified with other methods as well (e.g., Donlon et al. 2019; Gryncewicz et al. 2021; Donlon & Newberg 2022).

There are two classes of explanations for the origin of the Nyx stream with disparate effects on the terrestrial direct-detection experiments of dark matter. These two classes revolve around Nyx having an accompanying dark matter component, which reduces to whether Nyx is the remnant of one or more dwarf galaxy accretion events (Abadi et al. 2003; Sales et al. 2009; Read et al. 2009, 2008; Purcell et al. 2009; Ling et al. 2010; Pillepich et al. 2014; Rodriguez-Gomez et al. 2017). If Nyx is indeed a remnant of a merger, it would potentially contribute to a dark matter substructure, which could affect the local dark matter phase-space distribution and impact constraints from direct-detection experiments (Read et al. 2009; Bruch et al. 2009). Alternatively, Nyx could be a kinematic perturbation to the thick disk (e.g., van Donkelaar et al. 2022; Roš et al. 2008). This formation scenario would not contribute to the local dark matter phase-space distribution.

Chemical abundances of Nyx stars can distinguish between these formation scenarios because the chemical evolution causes stars from dwarf galaxies to have a distinct chemistry from the Milky Way (e.g., Venn et al. 2004). In particular, if Nyx is the remnant of an accreted dwarf galaxy, it should have a chemical composition similar to that of dwarf galaxies, e.g., low α abundances and evidence of the metal-poor *s*-process. By cross-matching with the RAVE-on chemical abundance catalog (Kunder et al. 2017; Casey et al. 2017), Necib et al. (2020b) found three metal-rich Nyx stars with Mg abundances $[\mathrm{Mg/Fe}] \lesssim 0.3$, which may be consistent with both the thick disk and accreted dwarf galaxy formation scenario. The inconclusive chemical abundance results arising from a combination of small sample size and large abundance errors motivate a higher-precision chemical abundance analysis of a larger sample of Nyx stars.

Recently, Zucker et al. (2021) analyzed the chemical abundances of 18 Nyx candidates from GALAH DR3 (Buder et al. 2021) and 9 candidates from APOGEE DR16 (Ahumada et al. 2020). The GALAH DR3 sample had $[\mathrm{Fe/H}] > -0.9$. Although the APOGEE DR16 sample mostly overlapped in this range, Zucker et al. (2021) identified two low-metallicity stars with $[\mathrm{Fe/H}] \sim -1.5$. They compared both samples with kinematically selected thick-disk stars, concluding that Nyx is chemically consistent with the thick disk. Horta et al. (2023) examined the chemical abundances of 589 stars consistent with Nyx kinematics from the APOGEE DR17 survey (Abdurro'uf et al. 2022). They identified a low-metallicity tail with $[\mathrm{Fe/H}] < -1.5$ in the sample, but did not provide further explanations for its existence. They also considered Nyx to be chemically similar to the in situ high-α thick disk. Both of these recent results suggest that Nyx could be a kinematic perturbation to the thick disk, although neither provides a plausible explanation for the existence of the metal-poor tail. This motivates further chemodynamic studies of the low-metallicity tail to unveil the origin of the Nyx stream.

In this paper, we study the chemodynamics of 34 Nyx stars observed with the Keck/HIRES and Magellan/MIKE spectrographs. We perform the first detailed analysis of the chemical abundances of the Nyx stars using a differential abundance analysis. Overall, we find that the chemical abundances of most Nyx stars are similar to those in the thick disk, consistent with previous studies. However, we also identify 5 stars that populate a highly eccentric metal-poor tail ($[\mathrm{Fe/H}] \sim -2.0$), which is not typically associated with the thick disk. This low-metallicity tail could be key to unveiling the origin of the Nyx stream, be it the remnant of multiple dwarf galaxy mergers or an unusual kinematic structure formed in the early turbulent Galactic disk.

Throughout this paper, we use v_r, v_ϕ, and v_θ to denote galactocentric velocities in spherical coordinates. The paper is organized as follows: Section 2 provides details of the observation and target selection. Section 3 introduces the methods we used to analyze the chemical abundances of the Nyx stars. Section 4 presents the chemical abundance results, which are compared to the thick-disk sample from Bensby et al. (2014) and highlight the fact that Nyx contains a metal-poor tail. Section 5 studies the kinematics of the Nyx stars. Section 6 discusses possible origins of the Nyx stream as well as their implications on the local dark matter phase-space distribution. Section 7 concludes the paper.

2. Target Selection and Observations

To identify accreted substructures, Necib et al. (2020a) performed a Gaussian mixture model analysis on stellar velocities in a catalog of accreted stars with a neural network score $S > 0.95$ from Ostdiek et al. (2020; see Section 1 for a summary). The Nyx stars are characterized by a Gaussian velocity distribution with mean $\{v_r, v_\phi, v_\theta\} = \{134, 130, 53.0\}$ km s^{-1} and dispersion $\{\sigma_r, \sigma_\phi, \sigma_\theta\} = \{67.2, 45.8, 66.3\}$ km s^{-1} (Necib et al. 2020b). We select 34 out of 94 stars from this velocity cluster with the highest probabilities of belonging to the Nyx velocity cluster. This biases our sample toward higher velocities and a smaller velocity dispersion compared to the full Nyx sample. The mean velocities of the Nyx sample studied in this paper are $\{v_r, v_\phi, v_\theta\} = \{167, 172, 44.4\}$ km s^{-1}, with dispersions $\{\sigma_r, \sigma_\phi, \sigma_\theta\} = \{55.0, 30.9, 59.0\}$ km s^{-1}.

We obtained high-resolution spectroscopy of these 34 Nyx stars: 28 stars on 2020 August 1, with the $0\farcs5$ slit using the Keck/HIRES spectrograph ($R \sim 67$k at 4100 Å; Vogt et al. 1994), and 6 stars on 2021 January 3 or 2021 July 28 (Nyx122147) with the $0\farcs5$ slit using the Magellan/MIKE spectrograph ($R \sim 50$k/40k on the blue/red arm of MIKE; Bernstein et al. 2003). The HIRES spectra range from 3650 to

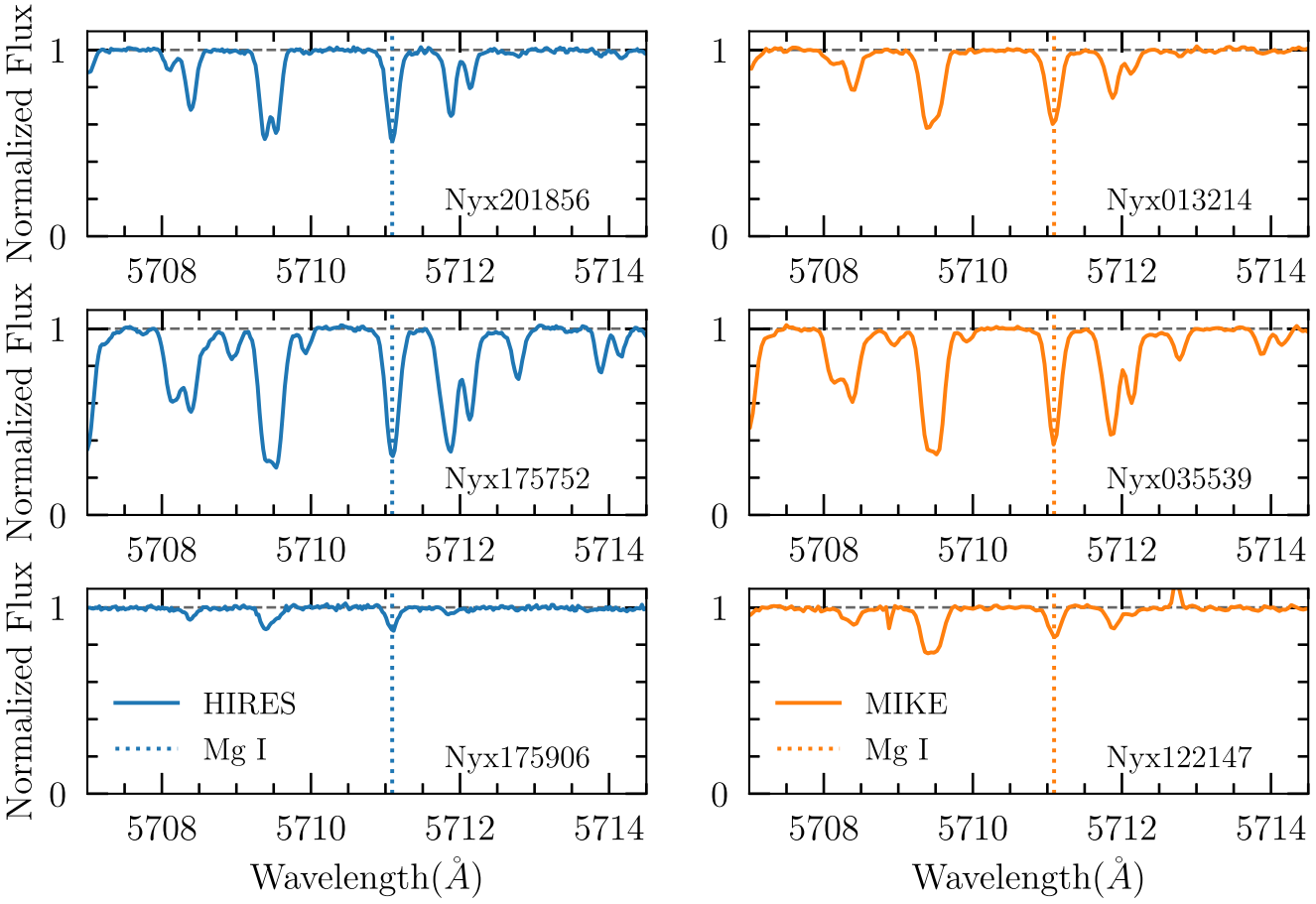

Figure 1. Spectra of the selected Nyx stars observed with HIRES (blue) or MIKE (orange) around the Mg I line at 5711 Å (dashed vertical lines). The stars are selected and sorted based on star type and metallicity. From top to bottom, the star in each subplot is a metal-rich dwarf, a metal-rich giant, or a metal-poor star.

8160 Å, and the MIKE spectra range from 3300 to 9400 Å. The portion of the spectra we used for the abundance analysis ranges from 4000 to 7000 Å. Figure 1 shows spectra around the Mg I line at 5711 Å for a few metal-rich dwarf, metal-rich giant, and metal-poor Nyx stars observed with HIRES and MIKE. The data for the 28 Nyx stars observed with HIRES were reduced with MAKEE v6.4,[12] while the data for the 6 stars observed with MIKE were reduced with CarPy (Kelson 2003).

We use the thick-disk stars from Bensby et al. (2014) as a comparison chemical and kinematic sample. Bensby et al. (2014) obtained high-resolution spectroscopy of 714 F and G dwarf stars in the solar neighborhood that traced multiple nearby kinematic components of the Milky Way (thin disk, thick disk, stellar halo, and streams). The selection function for these stars was purposely biased to probe as many Galactic components and the widest metallicity ranges of these components as possible. These stars were kinematically classified into thin-disk, thick-disk, and halo stars using the Gaussian velocity distributions defined in Bensby et al. (2003). We select 201 thick-disk stars with a ratio of the thick disk to the halo of TD/H > 2 and a ratio of the thick disk to the disk TD/D > 2.[13] We expect there to be 6 contaminating stars (3.0%) from the halo in this sample. Cross-matching these thick-disk stars with the accreted catalog from Ostdiek et al. (2020), we find that the neural network scores of these thick-disk stars is $S < 0.05$. Given the difference in scores, we expect there to be no contamination from kinematically ordinary thick-disk stars in our 34-star Nyx sample.

We determine chemical abundances differentially (see Section 3.4), so we select two stars from the Bensby et al. (2014) thick-disk sample to use as abundance references: the metal-rich reference star HIP88622, and the metal-poor reference star HIP7162. HIP88622 was observed on 2020 August 1 with the 0.″5 slit using the Keck/HIRES spectrograph (signal-to-noise ratio (S/N) per pixel ∼250 at 6500 Å). HIP7162 was observed on 2022 June 30 with the 0.″5 slit using the MIKE/Magellan spectrograph (S/N ∼ 114 at 6500 Å). For the reference star Arcturus, high-resolution spectra were obtained from Hinkle et al. (2000).

Table 1 lists the name, Gaia DR3 source ID, R.A./decl., observation date, instrument, Gaia G magnitude, exposure time (t_{exp}), S/N at 6500 Å, and heliocentric radial velocity (v_{hel}) of the observed Nyx stars. The last two columns of Table 1 provide the neural network score (S) of a star from Ostdiek et al. (2020), as well as its probability of belonging to the Nyx velocity distribution from Necib et al. (2020b). Radial velocities were measured by cross-correlating with a MIKE spectrum of the metal-poor giant HD122563 around Mgb. For stars that were observed with multiple exposures, we report the heliocentric velocity measured in the middle of the observation. The formal velocity uncertainties are 0.1–0.2 km s^{-1}, but past experience shows that the typical systematic error on the

[1] https://sites.astro.caltech.edu/~tb/makee/

[2] Changing the cut on TD/H from 2 to 10 only removes 6 stars out of 201 from the thick-disk sample.

Table 1
Observations

Name	Source id (Gaia DR3)	R.A. (deg)	Decl. (deg)	Obs Date	Instrument	G (mag)	t_{exp} (s)	S/N (6500 Å)	v_{hel} (km s^{-1})	Score	Velocity Probability
NYX004259	367439335551722240	10.74511785	37.38043004	2020-08-1	HIRES	10.74	350	151	24.6	0.97	0.77
NYX010249	314182978031619328	15.70439781	32.12158685	2020-08-1	HIRES	11.69	900	151	26.2	0.98	0.76
NYX010842	306730075901451520	17.17457698	26.70320141	2020-08-1	HIRES	11.70	900	159	27.1	0.96	0.78
NYX013214	4916946665759118720	23.06001744	−51.90289781	2021-01-3	MIKE	10.18	1200	140	−16.2	0.97	0.97
NYX014107	317636063018105088	25.27974372	33.92092371	2020-08-1	HIRES	11.21	550	144	27.1	0.97	0.61
NYX014725	305238279140992896	26.85528438	32.42734287	2020-08-1	HIRES	8.88	70	145	27.4	0.96	0.89
NYX022545	5174773415097847296	36.43952571	−10.98901054	2020-08-1	HIRES	11.62	900	148	26.3	0.96	0.94
NYX035539	4665853149532721664	58.91244399	−71.36549004	2021-01-3	MIKE	11.04	4085	232	−4.0	0.95	0.95
NYX044831	4665093769251640704	72.13076827	−62.48367570	2021-01-3	MIKE	8.91	400	169	−4.4	0.98	0.96
NYX063721	5497838651784528000	99.33851551	−54.82999871	2021-01-4	MIKE	10.52	1600	213	1.4	0.97	0.80
NYX064943	5497618547596953472	102.43003976	−53.84094205	2021-01-3	MIKE	9.03	600	248	2.5	0.98	0.97
NYX122147	3521755401833022080	185.44804146	−15.12392540	2021-07-28	MIKE	11.48	1800	121	2.8	0.97	0.97
NYX163705	1312596465842920576	249.27099451	31.32412562	2020-08-1	HIRES	11.93	1000	144	−16.7	1.00	0.82
NYX175752	4609530533258729600	269.46600702	36.54835952	2020-08-1	HIRES	10.65	300	155	−9.6	0.97	0.95
NYX175906	1345377378530252032	269.77384034	42.85162989	2020-08-1	HIRES	12.33	1500	137	−7.6	0.98	0.97
NYX185206	2146631118469602944	283.02543696	53.80289724	2020-08-1	HIRES	9.67	180	190	−0.9	0.98	0.95
NYX185250	2103594068696931968	283.21008746	40.77249320	2020-08-1	HIRES	12.54	1800	149	−3.9	0.97	0.87
NYX195253	4195105698600078848	298.22200157	−9.45925775	2020-08-1	HIRES	12.46	1800	148	−5.6	0.97	0.93
NYX201634	2062121830140100992	304.14213600	39.18034350	2020-08-1	HIRES	11.27	600	159	3.4	0.98	0.88
NYX201856	2084248913225887104	304.73284567	48.34020559	2020-08-1	HIRES	11.91	1000	143	4.7	0.97	0.97
NYX204828	1751338782564204672	312.11838846	9.68257413	2020-08-1	HIRES	10.14	300	179	3.6	0.97	0.88
NYX205642	1757797833557540480	314.17519078	12.37187691	2020-08-1	HIRES	12.04	1200	155	5.0	0.96	0.94
NYX211145	1867283181371868544	317.93598233	35.27867523	2020-08-1	HIRES	11.71	900	162	8.6	0.98	0.94
NYX213012	1850722646463457920	322.55098693	31.10214042	2020-08-1	HIRES	12.44	1800	148	10.3	0.99	0.93
NYX214142	1797966051335964672	325.42542891	25.19027732	2020-08-1	HIRES	11.39	600	142	11.2	0.98	0.97
NYX215612	2695833495753971072	329.04880607	3.77654551	2020-08-1	HIRES	12.81	2160	134	11.2	0.96	0.91
NYX215744	1794930334091349632	329.43432692	23.58644105	2020-08-1	HIRES	10.72	350	150	12.8	1.00	0.96
NYX223035	2738050790890416384	337.64587000	18.37272779	2020-08-1	HIRES	11.33	600	147	16	0.96	0.91
NYX224245	2833632062543310848	340.68697508	19.16973836	2020-08-1	HIRES	10.83	400	142	17.2	0.98	0.95
NYX225510	2714860681911345280	343.79139075	9.53497180	2020-08-1	HIRES	11.16	1200	215	17.9	0.95	0.90
NYX230605	2815219469025808128	346.52177833	13.86879634	2020-08-1	HIRES	11.20	500	140	19.3	0.97	0.91
NYX230903	2385788396590080512	347.26428804	−23.09773201	2020-08-1	HIRES	11.67	900	150	14.1	0.97	0.87
NYX232032	2813625898720075264	350.13478016	13.36493995	2020-08-1	HIRES	9.05	80	153	20.5	0.96	0.93
NYX234631	2771034730974538624	356.62832066	14.41544640	2020-08-1	HIRES	12.58	1800	141	22.7	0.97	0.91

(This table is available in machine-readable form.)

Table 2
Line Measurements

Star	λ (Å)	ID	χ	log gf	EW	σ(EW)	FWHM (Å)	log $\epsilon_{i,\mathrm{ref}}$	d_i	e_i	$\delta_{i,T_{\mathrm{eff}}}$	$\delta_{i,\log g}$	δ_{i,ν_t}	$\delta_{i,[\mathrm{M/H}]}$
NYX201856	5778.45	26.0	2.59	−3.43	9.5	0.4	0.11	6.92	−0.35	0.02	+0.05	−0.00	−0.00	+0.01
NYX201856	5855.08	26.0	4.61	−1.48	8.7	0.4	0.15	6.96	−0.29	0.02	+0.03	+0.00	−0.00	+0.01
NYX201856	6027.05	26.0	4.08	−1.09	40.5	0.3	0.13	7.00	−0.31	0.01	+0.04	+0.00	−0.02	+0.02
NYX201856	6136.99	26.0	2.20	−2.95	47.2	0.3	0.13	7.02	−0.30	0.01	+0.06	+0.00	−0.03	+0.01
NYX201856	6151.62	26.0	2.18	−3.29	30.3	0.3	0.12	6.97	−0.31	0.01	+0.06	+0.00	−0.01	+0.01
NYX201856	6165.36	26.0	4.14	−1.47	21.1	0.3	0.12	6.97	−0.31	0.01	+0.03	+0.00	−0.01	+0.01
NYX201856	6173.33	26.0	2.22	−2.88	47.4	0.4	0.12	6.98	−0.30	0.01	+0.06	+0.00	−0.03	+0.01
NYX201856	6213.43	26.0	2.22	−2.48	62.8	0.4	0.14	6.92	−0.28	0.01	+0.07	+0.00	−0.04	+0.01
NYX201856	6271.28	26.0	3.33	−2.70	11.7	0.4	0.15	6.94	−0.24	0.02	+0.04	−0.00	−0.00	+0.01
NYX201856	6322.69	26.0	2.59	−2.43	52.6	0.4	0.14	7.03	−0.30	0.01	+0.06	+0.00	−0.03	+0.02
NYX201856	6335.33	26.0	2.20	−2.18	76.8	0.4	0.15	6.87	−0.25	0.01	+0.08	−0.00	−0.05	+0.01
NYX201856	6411.65	26.0	3.65	−0.60	89.2	0.5	0.17	6.89	−0.26	0.01	+0.06	−0.03	−0.03	+0.04
NYX201856	6518.37	26.0	2.83	−2.44	37.7	0.4	0.14	⋯	⋯	0.01	+0.05	+0.00	−0.02	+0.01
NYX201856	6581.21	26.0	1.49	−4.68	9.2	0.4	0.13	7.01	−0.42	0.02	+0.06	−0.00	−0.00	+0.01
NYX201856	6593.87	26.0	2.43	−2.42	62.2	0.4	0.15	7.02	−0.26	0.01	+0.07	+0.00	−0.04	+0.01
NYX201856	6609.11	26.0	2.56	−2.69	41.4	0.4	0.14	7.01	−0.32	0.01	+0.06	+0.00	−0.02	+0.01
NYX201856	6739.52	26.0	1.56	−4.79	7.5	0.4	0.18	6.89	−0.21	0.03	+0.06	−0.00	−0.00	+0.01
NYX201856	6810.26	26.0	4.61	−0.99	22.1	0.4	0.15	6.98	−0.34	0.01	+0.03	+0.00	−0.01	+0.02
NYX201856	6828.59	26.0	4.64	−0.82	27.6	0.4	0.16	6.98	−0.32	0.01	+0.03	+0.00	−0.01	+0.02
NYX201856	6837.01	26.0	4.59	−1.69	7.2	0.4	0.18	7.01	−0.26	0.03	+0.03	+0.00	−0.00	+0.01
NYX201856	6843.66	26.0	4.55	−0.73	31.7	0.3	0.14	6.88	−0.32	0.01	+0.03	+0.00	−0.01	+0.02

Note. A portion of this table is shown for form. The column details are provided in the text. The full version is available online.
(This table is available in its entirety in machine-readable form.)

velocity due to wavelength calibration and template mismatches is 1.0 km s^{-1} (e.g., Ji et al. 2020a).

3. Abundance Analysis

We determine the stellar abundances using the 2017 version of the 1D local thermodynamic equilibrium (LTE) radiative transfer code MOOG[14] with scattering (Sneden 1973; Sobeck et al. 2011). We use SMHR[15] to normalize and stitch echelle orders, fit equivalent widths, interpolate ATLAS model atmospheres (Castelli & Kurucz 2003), run MOOG, and perform spectral syntheses (as described in Casey 2014; Ji et al. 2020b). As described in the following subsections, stellar parameters are determined spectroscopically, and the final abundances are determined differentially relative to the reference stars from Bensby et al. (2014) and McWilliam et al. (2013).

3.1. Line List and Line Measurements

Our line list is primarily adopted from Jönsson et al. (2017), Lomaeva et al. (2019), and Forsberg et al. (2019), supplemented by Fe lines from Bensby et al. (2005; see Table 2), Na and Y lines from McWilliam et al. (2013), and Ti, Ni, and Y lines from Roederer et al. (2018). We individually examine each line, rejecting those with heavy blending issues, saturation, or nondetection. For the 28 Nyx stars observed with Keck/HIRES, some lines fall into chip gaps. These include some Fe and some Y lines.

We use a combination of equivalent widths and spectral synthesis to determine the stellar abundances. For equivalent widths, we use SMHR to fit a Gaussian or Voigt profile multiplied by a linear continuum to each absorption line. The equivalent width measurements are individually examined to flag problematic lines, remove heavily blended lines, and correct inaccuracies in local continuum fitting. We use equivalent widths to determine the abundances of Na I, Mg I, Si I, Ca I, Ti I, Fe I/II, Ni I, Zn I, Y II, and Ba II. For lines with hyperfine splitting (e.g., La II), we use synthetic spectra to determine the abundances. SMHR finds the best-fit synthetic spectra using chi-squared minimization (see details in Ji et al. 2020b). We individually inspect all synthetic fits to ensure accuracy.

3.2. Reference Stars for Differential Abundances

We adopt the method of differential abundance analysis, which minimizes systematic effects due to atomic data, stellar parameters, blended lines, and NLTE effects (e.g., Nissen & Schuster 2010; McWilliam et al. 2013; Matsuno et al. 2022).[16]

Our Nyx stars span a wide range of stellar parameters, so we adopt three different reference stars for our differential analysis: HIP7162, HIP88622, and Arcturus, which were analyzed in Bensby et al. (2014) and McWilliam et al. (2013). We use HIP7162 as the reference star for all metal-poor stars ([Fe/H] ~ -2.0), with reference abundances from Bensby et al. (2014); we use HIP88622 as the reference star for metal-rich dwarfs ([Fe/H] > -1.0, $T_{\mathrm{eff}} \gtrsim 5200$ K), with reference abundances from Bensby et al. (2014); and we use Arcturus as the reference star for the metal-rich giants ([Fe/H] > -1.0, $T_{\mathrm{eff}} \lesssim 5200$ K), with reference abundances from McWilliam et al. (2013) and Fanelli et al. (2021). The adopted stellar parameters for these reference stars are listed in Table 3.

3.3. Stellar Parameters

We derive stellar parameters spectroscopically, adopting ATLAS model atmospheres (Castelli & Kurucz 2003). We

[3] https://github.com/alexji/moog17scat
[4] https://github.com/andycasey/smhr/tree/py38-mpl313

[5] The coolest and most metal-rich Nyx185206 is removed from the differential abundance analysis because blending issues affect almost all elements of the star.

Table 3
Stellar Parameters

Star	$T_{\rm eff}$(K)	$\sigma(T_{\rm eff})$	log g (dex)	σ(log g)	ν_t(km s^{-1})	$\sigma(\nu_t)$	[M/H]	σ([M/H])	[α/Fe]	[Fe/H]$_{\rm d}$
NYX004259	6400	177	4.10	0.16	1.60	0.23	−0.45	0.11	0.30	−0.30
NYX010249	6154	280	3.90	0.20	1.01	1.05	−2.26	0.14	0.40	−2.20
NYX010842	4980	94	3.45	0.15	0.89	0.11	−0.50	0.13	0.40	−0.42
NYX013214	5296	97	4.07	0.17	0.82	0.24	−1.01	0.13	0.40	−0.86
NYX014107	5082	77	2.64	0.15	1.48	0.09	−0.75	0.12	0.40	−0.68
NYX014725	5120	90	3.09	0.16	1.19	0.09	−0.31	0.12	0.40	−0.22
NYX022545	4734	100	2.92	0.18	1.16	0.10	−0.39	0.13	0.40	−0.32
NYX035539	4513	74	2.22	0.16	1.43	0.09	−0.74	0.12	0.40	−0.67
NYX044831	5314	69	2.60	0.15	1.70	0.11	−0.93	0.11	0.40	−0.86
NYX063721	4984	76	2.77	0.16	1.38	0.09	−0.56	0.12	0.40	−0.47
NYX064943	4638	87	2.12	0.17	1.50	0.09	−0.44	0.13	0.40	−0.36
NYX122147	4652	71	1.54	0.15	1.32	0.15	−2.19	0.13	0.40	−2.13
NYX163705	5530	88	4.54	0.16	0.85	0.20	−0.60	0.12	0.40	−0.47
NYX175752	4445	69	2.04	0.21	1.61	0.09	−0.57	0.12	0.40	−0.49
NYX175906	5870	117	3.85	0.19	0.85	0.64	−1.78	0.14	0.40	−1.71
NYX185250	5228	75	2.89	0.16	1.59	0.10	−0.74	0.12	0.40	−0.66
NYX195253	5623	93	3.85	0.16	1.12	0.14	−0.70	0.12	0.40	−0.56
NYX201634	4933	70	3.10	0.15	1.08	0.08	−0.75	0.12	0.40	−0.67
NYX201856	5402	68	3.71	0.15	0.90	0.11	−0.84	0.11	0.40	−0.70
NYX204828	4541	70	2.21	0.16	1.37	0.09	−0.80	0.12	0.40	−0.71
NYX205642	5135	71	3.73	0.15	1.07	0.09	−0.55	0.11	0.40	−0.47
NYX211145	4884	75	3.07	0.16	1.27	0.09	−0.66	0.12	0.40	−0.58
NYX213012	5003	76	2.52	0.15	0.91	0.17	−2.14	0.12	0.40	−2.08
NYX214142	5188	69	2.75	0.15	1.49	0.09	−0.83	0.11	0.40	−0.74
NYX215612	5789	111	4.22	0.15	1.26	0.21	−0.63	0.12	0.40	−0.51
NYX215744	4990	85	3.65	0.16	0.92	0.12	−0.28	0.12	0.40	−0.20
NYX223035	4905	73	2.72	0.16	1.31	0.09	−0.45	0.12	0.40	−0.38
NYX224245	4985	114	3.67	0.15	0.80	0.14	−0.21	0.13	0.40	−0.13
NYX225510	5584	86	3.84	0.15	1.10	0.13	−0.79	0.11	0.40	−0.66
NYX230605	6501	118	3.84	0.17	1.40	0.19	−0.56	0.11	0.25	−0.42
NYX230903	5401	68	3.55	0.16	0.96	0.11	−1.41	0.11	0.30	−1.35
NYX232032	5032	74	3.16	0.16	1.14	0.09	−0.88	0.12	0.40	−0.80
NYX234631	5612	121	3.70	0.17	0.79	0.28	−0.96	0.13	0.40	−0.82
Arcturus	4290	119	1.60	0.31	1.60	0.22	−0.50	0.14	0.40	−0.49
HIP7162	5217	92	2.97	0.16	1.60	0.49	−2.05	0.12	0.40	−2.05
HIP88622	5754	80	4.32	0.15	1.00	0.13	−0.53	0.11	0.40	−0.40

Note. Stellar parameters of the Nyx stars. [X/Fe]d refers to the differential Fe abundance, which differs from the model metallicity [M/H]. See Section 3.2 for more details.

(This table is available in machine-readable form.)

balance the excitation potential and line strength against differential Fe I abundances to derive the effective temperature, $T_{\rm eff}$, and microturbulence, ν_t, of the Nyx stars. We balance the ionization states for differential Fe I and Fe II to derive the surface gravity, log g. The model metallicity of Nyx stars is set to differential [FeI/H]. We set [α/Fe] to [Ca/Fe]. The differential line abundance of each element for each Nyx target is determined as follows: we match the individual lines and calculate the abundance differences between the target and the reference star. We add the reference abundance to the line abundance difference to derive the differential line abundance. The final differential abundance of each element is derived by adding the reference abundance to the average line-abundance difference.

For the most metal-poor star Nyx010249, we are unable to effectively constrain its microturbulence, so we determine it by fitting a polynomial to the log g − ν_t relation of the other Nyx stars, $\nu_t = 0.053(\log g)^2 - 0.47 \log g + 2.08$.

Stellar parameter uncertainties include a combination of statistical and systematic uncertainties. Statistical uncertainties are determined for the 1σ standard error on the slopes of abundance differences (see Ji et al. 2020b for details). Systematic uncertainties are estimated by comparison to photometric stellar parameters using Gaia DR3 broadband photometry (Gaia Collaboration et al. 2023). The photometric effective temperature of each star is determined using the color $-T_{\rm eff}$ relation (Mucciarelli et al. 2021). The microturbulence and model metallicity are determined using SMHR, and are individually examined to ensure accuracy. The final systematic uncertainties are 50 K, 0.15 dex, 0.10 km s^{-1}, and 0.05 dex for $T_{\rm eff}$, log g, ν_t, and [M/H], respectively, for metal-rich dwarfs; 100 K, 0.30 dex, 0.10 km s^{-1}, and 0.20 dex for metal-rich giants; and 200 K, 0.40 dex, 0.10 km s^{-1}, and 0.20 dex for metal-poor stars.

Table 3 shows the stellar parameters of the Nyx and reference stars, HIP88622, HIP7162, and Arcturus. Each row provides the stellar $T_{\rm eff}$, log g, ν_t, the model metallicity ([M/H]), α abundance ([α/Fe]), and the differential Fe abundance

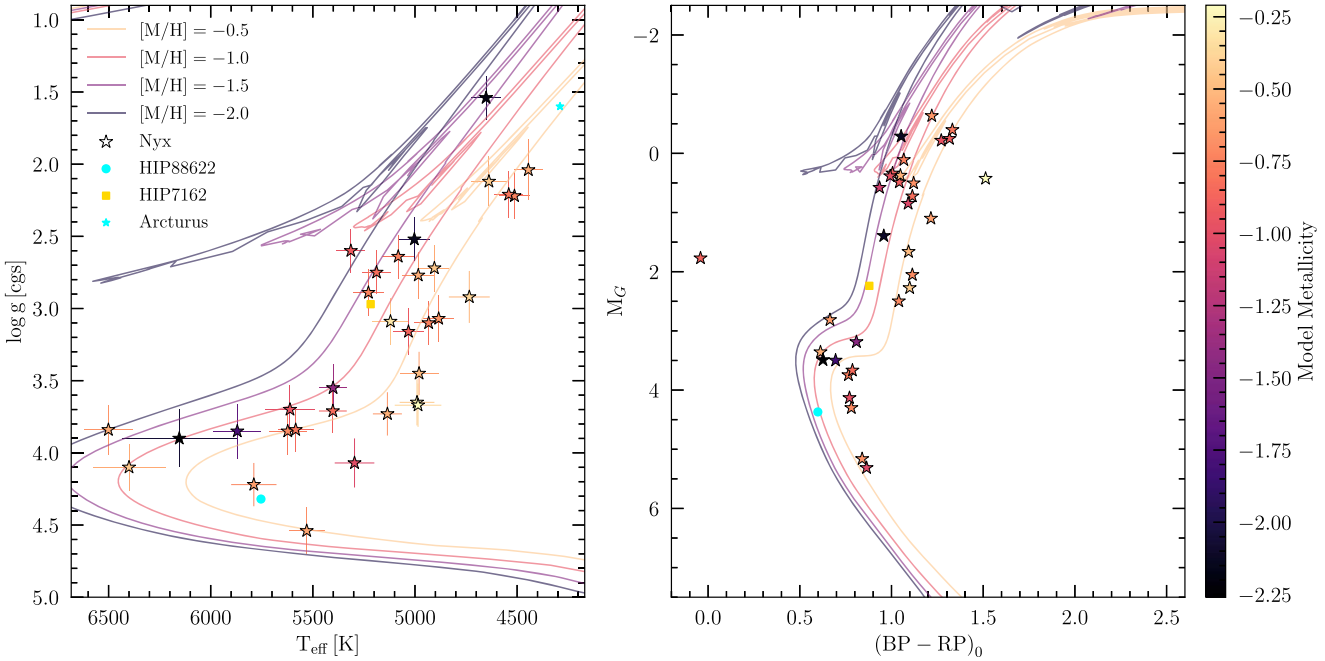

Figure 2. Kiel diagram (left) and color-magnitude diagram (right) of the observed Nyx stars. Nyx stars are color-coded by model metallicity. MIST isochrones with age 10 Gyr and [M/H] $\in$ [−2.0, −0.5] (Choi et al. 2016) are plotted for comparison. The reference stars HIP7162, HIP88622, and Arcturus used in Section 3.2 are indicated by the gold square, the cyan dot, and the star, respectively. The plot demonstrates that the Nyx sample is composed of slightly metal-poor dwarf and giant stars, with five Nyx stars having distinctly lower model metallicity.

([Fe/H]^d).[17] Uncertainties $\sigma(X)$ are provided for the first four of these quantities; uncertainties on [α/Fe] are not propagated, but are negligible. Figure 2 shows the Kiel and Gaia DR3 color-magnitude diagrams of the Nyx and two of the reference stars.[18] In the color-magnitude diagram, reddening is corrected using $E(B-V)$ from Schlafly & Finkbeiner (2011) [19] and transformed into G, BP, and RP magnitudes using the Gaia DR3 extinction coefficients.[20] To guide the eye, we show MIST isochrones (Choi et al. 2016) with the age set at 10 Gyr and covering the metallicity range [−2.0, −0.5]. The plot demonstrates that the sample stars are composed of slightly metal-poor dwarf and giant stars. The metallicity of most Nyx stars falls in the range [M/H] $\in$ [−1.0, −0.5], but five stars have a metallicity [M/H] ~ -2.0. Compared to the Nyx targets in Necib et al. (2020b), those in this work contain more metal-rich giants.

3.4. Abundance Uncertainties

Differential abundance uncertainties were calculated using the method introduced in McWilliam et al. (2013). The abundance uncertainty for each species is

$$\sigma^2 = \sigma_{\rm rand}^2 + \sigma_{\rm sys}^2 + \sigma_{\rm sp}^2 = \frac{1}{\sum_i^N 1 \Big/ e_i^2} + \frac{1}{N}\sum_i^N (d_i - \langle d \rangle)^2 + \sum_X \left(\frac{1}{N}\sum_i^N \delta_{i,X} \right)^2, \quad (1)$$

where i is the index of a line for the species, N is the total number of lines for the species, e_i is the statistical uncertainty, d_i is the line-by-line abundance difference relative to the reference star, $\langle d \rangle$ is the mean line-by-line abundance difference, X is the stellar parameter ($T_{\rm eff}$, $\log g$, ν_t, and [Fe/H]), and $\delta_{i,X}$ is the stellar parameter uncertainty difference (see Table 2). The individual terms of Equation (1) are provided in Table 4. The first term on the right-hand side of the equation is the squared average uncertainty due to random spectrum noise; the second term is the squared average systematic uncertainty as measured by the line-to-line standard deviation; and the third term is the squared uncertainty due to stellar parameters. We regard the precision of our abundance measurements to be $\sqrt{\sigma_{\rm rand}^2 + \sigma_{\rm sys}^2}$ ($\sigma_{\rm [X/Fe]d}$ in Table 4). The accuracy of our abundances should further add the stellar parameter uncertainty in quadrature. Note that the covariance between stellar parameters is included in McWilliam et al. (2013), but is not considered in this paper, which tends to overestimate the abundance uncertainties for [X/Fe] ratios (see Ji et al. 2020b for details).

Table 2 lists the individual measurements for each line in our line list. As an example, the portion of the table printed here lists the Fe I line measurements of Nyx201856. Each row contains the name of the star, the wavelength of the line (λ), the

[6] The differential Fe abundance [Fe/H]$_{\rm d}$ is shown to contrast with the model metallicity [M/H] derived by balancing iron abundances, and it is henceforth referred to exclusively as the metallicity.
[7] The reference star Arcturus is not in Gaia DR3.
[8] Obtained from the IPAC dust map (IRSA 2022).
[9] https://www.cosmos.esa.int/web/gaia/edr3-extinction-law

Table 4
Stellar Abundances

Star	El.	N	$[X/H]_d$	$[X/Fe]_d$	$\sigma_{[X/Fe]d}$	$[X/H]_{ref}$	$\sigma_{[X/H]ref}$	$[X/Fe]_{ref}$	σ_{rand}	σ_{sys}	σ_{sp}
NYX201856	Na *I*	4	−0.68	0.02	0.06	−0.37	0.02	0.03	0.00	0.04	0.04
NYX201856	Mg *I*	4	−0.34	0.36	0.06	−0.15	0.02	0.25	0.00	0.02	0.06
NYX201856	Si *I*	6	−0.55	0.14	0.12	−0.23	0.03	0.17	0.00	0.12	0.03
NYX201856	Ca *I*	7	−0.46	0.24	0.07	−0.29	0.02	0.11	0.00	0.02	0.07
NYX201856	Ti *I*	25	−0.37	0.33	0.09	−0.19	0.01	0.21	0.00	0.05	0.07
NYX201856	Fe *I*	20	−0.70	0.00	0.07	−0.40	0.01	0.00	0.00	0.04	0.06
NYX201856	Fe II	5	…	…	0.11	…	…	…	0.01	0.05	0.09
NYX201856	Ni *I*	12	−0.69	0.01	0.07	−0.40	0.01	0.00	0.00	0.04	0.06
NYX201856	Zn *I*	2	−0.53	0.17	0.08	−0.22	0.02	0.18	0.01	0.02	0.08
NYX201856	Y II	3	−0.66	0.04	0.10	−0.56	0.03	−0.16	0.01	0.05	0.09
NYX201856	Ba II	3	−0.68	0.02	0.10	−0.47	0.04	−0.07	0.00	0.04	0.10

Note. One star from this table is shown for form. Column details are provided in the text. The full version is available online.

(This table is available in its entirety in machine-readable form.)

element species (ID), the excitation potential (χ) and oscillator strength ($\log gf$), the equivalent width and the uncertainty (EW, σ(EW)), the full width at half maximum (FWHM), the measured abundance of the reference star ($\log \epsilon_{i,ref}$), the abundance difference (d_i), the statistical uncertainty (e_i), and the stellar parameter abundance differences ($\delta_{i,X}$), where X is a stellar parameter.

The differential abundances and uncertainties are given in Table 4. The differential abundances of Nyx201856 are measured with respect to the reference star HIP88622. In the table, each row contains the name of the star; the element measured (El.); the number of lines used (N); the derived differential abundances [X/H] (relative to the solar abundance; Asplund et al. 2009) and [X/Fe] with respect to HIP88622 ($[X/H]_d$, $[X/Fe]_d$), and the uncertainty $\sigma_{[X/Fe]d}$; the [X/H] value for the reference star and uncertainty ($[X/H]_{ref}$, $\sigma_{[X/H]ref}$); the [X/Fe] value for the reference star ($[X/Fe]_{ref}$); the uncertainty due to the random spectrum noise σ_{rand}, the systematic uncertainty σ_{sys}, and the uncertainty due to stellar parameters σ_{sp}.

We used spectroscopic stellar parameters to derive the abundances, but for verification, we also determined the differential abundances of the Nyx stars using photometric stellar parameters. For most elements, the differential abundances measured with photometric stellar parameters have a slightly larger standard deviation (∼0.02 dex) than those measured with spectroscopic stellar parameters. The conclusions in Section 7 remain the same regardless of the use of spectroscopic or photometric stellar parameters because any systematic stellar parameter uncertainties should be accounted for in our error analysis.

We also determined absolute abundances, which allowed us to measure a few more additional elements that were not measured in Bensby et al. (2014); see Appendix.

3.5. Discussion of Individual Element Abundances and Lines

We now discuss the selection of lines for the elements included in the differential abundance analysis. For metal-rich giants, the selected lines are checked for blending issues using visual inspection (magnesium and titanium) or by comparing against spectral synthesis (yttrium). The selected lines are examined for saturation using their reduced equivalent widths (REW) and by visual inspection. Saturated lines are fitted with Voigt profiles.

Iron. We measure up to 29 Fe I and Fe II lines in most Nyx stars. Fe I lines are used to determine the stellar parameters and model metallicities of the Nyx stars. Fewer Fe lines from the Jönsson et al. (2017) line list could be measured for the metal-poor ([Fe/H]∼ −2.0) stars. Therefore, additional lines from Bensby et al. (2005) are added to enable a stellar parameter and metallicity determination. Because we balance the ionization states to determine $\log g$, the [FeI/H] and [FeII/H] we measure usually differs by less than 0.05 dex.

Sodium. Na I is measured using up to four lines, including the Na doublet at 6154 Å and 6160 Å.

Magnesium. Equivalent widths of up to six Mg I lines, including the lines at 6318 and 6319 Å,[21] are measured in most Nyx stars. The Mg line at 4702 Å is usually saturated.

Silicon. Equivalent widths of six Si I lines are measured in most Nyx stars.

Calcium. Ca has the smallest uncertainties out of the α-elements and is used as the reference α element to determine the stellar parameters of the Nyx stars. Equivalent widths of seven Ca I lines are measured in a typical Nyx star. Ca lines at 6122 Å, 6162 Å, and 6439 Å are usually saturated.

Titanium. We determine Ti I abundances by equivalent width measurements of up to 25 Ti I lines.

Nickel. We measure the equivalent widths of up to 12 Ni I lines. Because the Ni abundances were not determined in McWilliam et al. (2013), the reference Ni abundance of Arcturus is instead taken from Fanelli et al. (2021). We add an uncertainty of 0.1 dex (approximately the difference between the [Fe/H] of Arcturus in McWilliam et al. 2013 and that in Fanelli et al. 2021) to the final Ni abundances to account for the offset (the zeropoint uncertainty; see Figure 3).

Zinc. Two Zn lines are measured at 4722 and 4810 Å using equivalent widths. Because Zn is not measured for the reference star HIP7162, we are unable to determine the differential abundances of Zn for the metal-poor Nyx stars. The reference Zn abundance of Arcturus is taken from Fanelli et al. (2021), and an uncertainty of 0.1 dex is added to the final Zn abundances to account for the zeropoint uncertainty.

Yttrium. In general, up to six Y II lines are measured using equivalent widths. For the very cool metal-rich giant reference star Arcturus ([Fe/H] = −0.49, T_{eff} = 4290 K), only the Y

[10] We fit the local continuum around the Mg lines at 6318 and 6319 Å, including the depression from the Ca I auto-ionization feature.

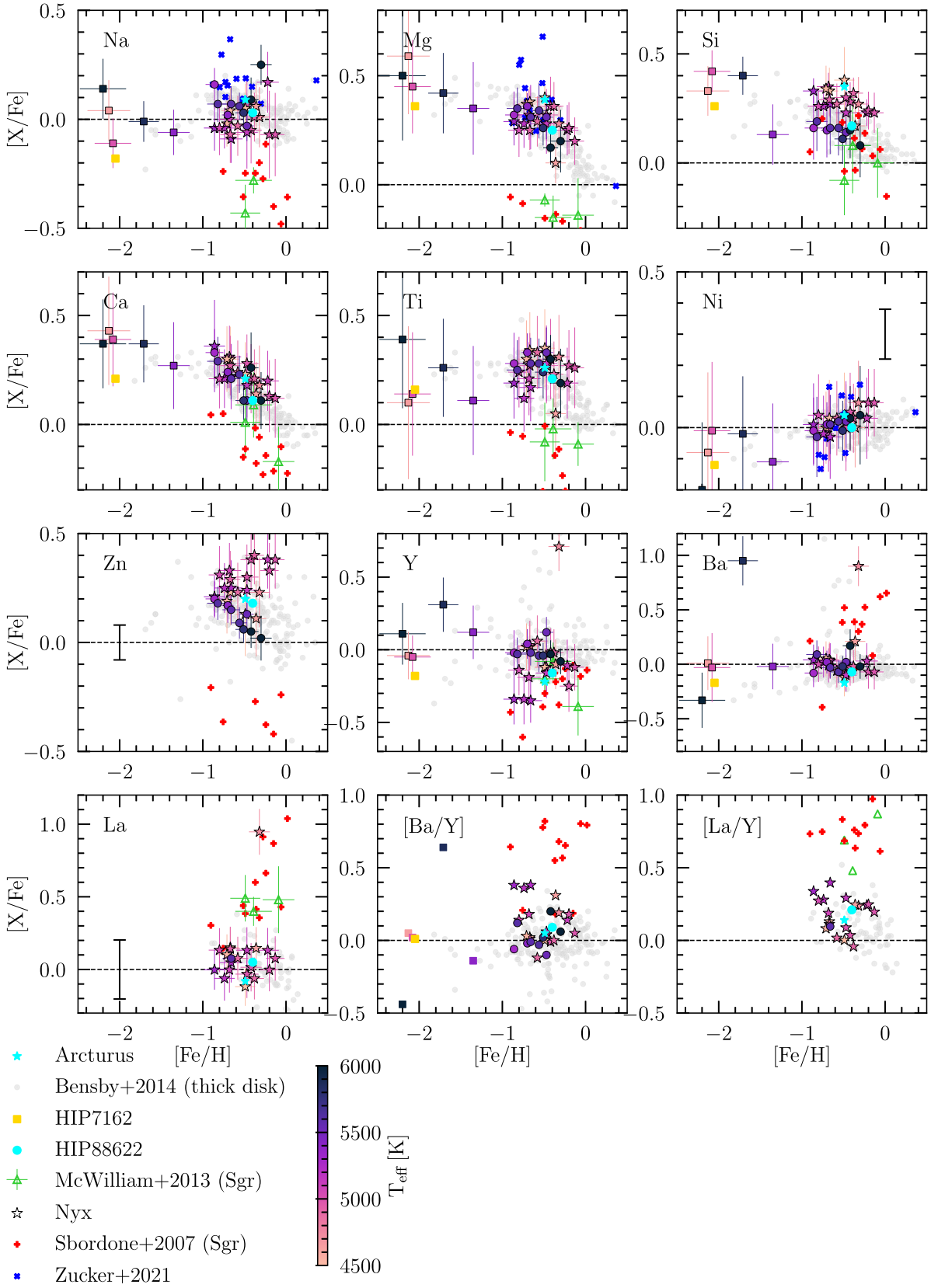

Figure 3. Differential chemical abundances ([X/Fe] vs. [Fe/H]. The *y*-axis is [X/Fe], except when another ratio is indicated) of metal-rich Nyx dwarfs (dots) relative to HIP88622 (cyan dot), giants (stars, labeled "Nyx") relative to Arcturus (cyan star), and metal-poor stars (squares) relative to HIP7162 (gold square), color-coded by effective temperature. For Na, Mg, and Ni, 18 Nyx stars selected by Zucker et al. (2021) from GALAH DR3 are plotted as blue crosses. The abundances of thick-disk stars (light gray dots) are from Bensby et al. (2014), except for the La abundances, which are from Battistini & Bensby (2016). The abundances of three Sgr dwarf galaxy stars from McWilliam et al. (2013) are indicated by the green triangles, while those of 12 Sgr stars from Sbordone et al. (2007) are indicated by the red plusses. A dashed line at [X/Fe] = 0.0 is shown as a reference. The black error bar in the Ni, Zn, and La abundance panel indicates the zeropoint uncertainty. In general, the chemical abundances of the metal-rich Nyx component are consistent with the thick disk and distinct from the Sgr dwarf galaxy.

lines at longer wavelengths ($\lambda \gtrsim 5200$ Å) could be measured reliably.

Barium. Abundances of three Ba II lines are measured using equivalent widths. We verify that including hyperfine splitting does not significantly affect the Ba abundances.

Lanthanum. La II abundances are derived by synthesizing the line at 6391 Å, which has hyperfine splitting and is only available in the metal-rich Nyx stars. For metal-rich giants, the differential La abundances are measured with respect to Arcturus, whose reference abundance is taken from McWilliam et al. (2013). Although Bensby et al. (2014) did not determine the La abundances, the same group measured the La abundances in Battistini & Bensby (2016) for a subset of their thick-disk stars. Unfortunately, Battistini & Bensby (2016) did not measure La for our reference star HIP88622. To estimate the differential La abundance for metal-rich dwarfs, we instead assume that the La abundance of HIP88622 is identical to HIP16365, which has nearly identical stellar parameters. The La abundance of HIP16365 is measured using the different 4662 Å line, so we estimate an uncertainty of HIP88622 (see Figure 3) using the standard deviation of the La abundance measurements for the 4662 Å line in Battistini & Bensby (2016).

4. Abundance Results

Table 4 presents the final abundances of each Nyx star. Figure 3 shows the abundance comparison of Nyx stars with thick-disk stars from Bensby et al. (2014). We highlight the reference stars Arcturus, HIP88622 and HIP7162, which are used for the differential abundance analysis of the 19 metal-rich giants ([Fe/H]> -1.0, $T_{\rm eff} \lesssim 5200$ K), nine metal-rich dwarfs ([Fe/H]> -1.0, $T_{\rm eff} \gtrsim 5200$ K), and five metal-poor ([Fe/H]~ -2.0) Nyx stars, respectively. The stars are color-coded by $T_{\rm eff}$ to highlight possible systematic issues. Figure 3 also shows the abundances of Nyx stars from GALAH DR3 (Zucker et al. 2021), which we note are not on exactly the same differential abundance scale. We use chemical abundances of three Sagittarius (Sgr) dwarf galaxy stars from McWilliam et al. (2013) and 12 Sgr stars from Sbordone et al. (2007) to illustrate the expected abundance differences between metal-rich dwarf galaxy stars and thick-disk stars.

A quick glance at Figure 3 shows that most Nyx stars are relatively metal rich ([Fe/H]~ -0.5), but five stars have [Fe/H] ~ -2.0. The detailed chemical abundances of these metal-poor Nyx stars were not previously discussed (Necib et al. 2020b; Zucker et al. 2021; Horta et al. 2023). In what follows, we discuss the chemical abundances of the metal-rich and metal-poor component of Nyx separately.

4.1. Metal-rich Component

Overall, the metal-rich Nyx component is consistent with the thick disk and distinct from dwarf galaxies. Specifically, Nyx stars have high α abundances and do not show evidence of the metal-poor *s*-process.

Odd-Z element (Na). The metal-rich Nyx stars average [Na/Fe] = 0.02, with a dispersion of 0.08 dex. Figure 3 demonstrates that the Na abundances of the metal-rich Nyx stars are consistent with the thick-disk stars within ∼0.1 dex. The Na abundances are also much higher (by ∼0.3 dex) than those of the Sgr dwarf galaxy stars.

α-elements (Mg, Si, Ca, and Ti). Figure 3 shows that the metal-rich Nyx stars have high α abundances with a slightly downward trend with [Fe/H], which is consistent with the high-α thick disk. The α abundances of the metal-rich Nyx stars are inconsistent with metal-rich dwarf galaxies—typically 0.2 −0.4 dex higher than those of the Sgr stars. There may appear to be an overlap between the α abundances of Nyx and Sgr stars at the highest metallicity, but in this region, the most metal-rich thick-disk stars have similar α abundances as well. Figure 3 illustrates that the Mg abundances of the metal-rich Nyx component has a plateau at [Fe/H]$\lesssim -0.5$ and a slightly downward trend at higher metallicities. This agrees with the Nyx abundances reported in Zucker et al. (2021) and Horta et al. (2023), but it differs from the RAVE-on Mg abundances reported in Necib et al. (2020b), which were lower and did not show this trend. Zucker et al. (2021) pointed out that this is likely due to the low precision in the RAVE-on Mg abundance measurements. For the metal-rich giants, the large uncertainties in the Ti abundances are mainly systematic uncertainties ($\delta_{T_{\rm eff}} \sim 0.17$) resulting from the large $T_{\rm eff}$ uncertainties (∼100 K on average).

Iron-peak elements (Ni and Zn). The iron-peak abundances have a relatively small dispersion of 0.03 dex (Ni) and 0.1 dex (Zn). In Figure 3, the [X/Fe] ratios of iron-peak elements do not display significant trends with respect to [Fe/H]. The Ni abundances from GALAH DR3 (Zucker et al. 2021) have a larger scatter than our differential abundances for Ni, but the overall trend remains flat. Figure 3 shows relatively large uncertainties in the Ni and Zn abundance measurements. These are mainly systematic uncertainties ($\delta_{\log g} \sim 0.15$) resulting from the large $\log g$ uncertainties (∼0.3 dex). In general, the abundances of the iron-peak elements for the metal-rich Nyx stars are all consistent with the thick-disk stars.

Neutron-capture elements (Y, Ba, La, and Eu). Most metal-rich Nyx stars have [Y/Fe] and [Ba/Fe] ∼ 0.0, similar to the thick disk, although there appears to be a substantial scatter around this mean (0.19 dex for Y and 0.18 dex for Ba). In Figure 3, the average Y abundances of the metal-rich dwarfs are higher by ∼0.3 dex when compared to the Sgr dwarf galaxy stars.

Some of the Ba scatter might be expected from inhomogeneous *s*-process enrichment or binary mass transfer from an asymptotic giant branch (AGB) companion (e.g., Cseh et al. 2022). In order to evaluate the binary nature of the Nyx stars, we compare our observed radial velocities with Gaia DR3 results (Gaia Collaboration et al. 2023). We find three Nyx stars with radial velocity variations more than 4.2 km s^{-1} (3 σ). One of these stars is the metal-rich star Nyx022545, which also has a very high Ba abundance ([Ba/Fe] ∼ 1.0.) These stars could potentially be in close binaries (e.g., Monaco et al. 2007). The metal-poor star Nyx175906 with a relatively high [Ba/Fe], however, has an observed radial velocity consistent with Gaia DR3, which cannot determine its binary nature. The [Ba/Y] ratios of the metal-rich component also broadly match the thick disk, in contrast to dwarf galaxies, which are expected to have higher [Ba/Y] ratios (∼0.7; Venn et al. 2004; McWilliam et al. 2013).

Figure 3 indicates that the La abundances of the Nyx stars are roughly constant as a function of metallicity, and they are ≳0.4 dex lower than those of the Sgr dwarf galaxy stars. The [La/Y] ratios of the Sgr stars are also much higher, characteristic of the ratio of heavy to light neutron-capture

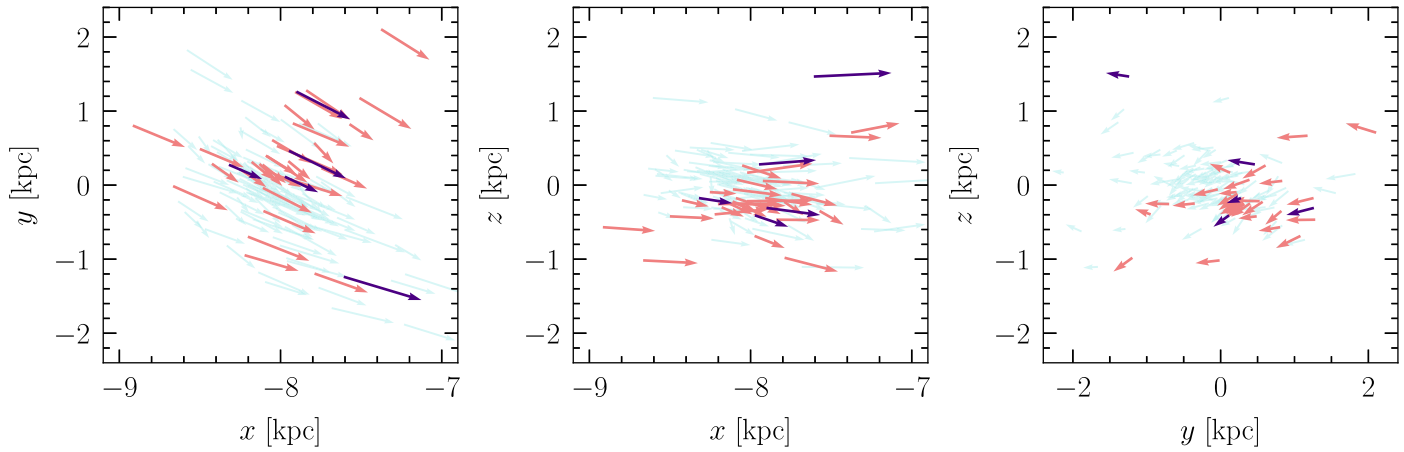

Figure 4. Spatial distributions of Nyx stars observed with high-resolution spectroscopy in this paper. The velocities are shown as arrows, where the length of the arrow is proportional to the speed of the stars in that projection (e.g., in the first panel, the length of the arrow is proportional to $\sqrt{v_x^2 + v_y^2}$). The observed stars in this paper are shown in peach, and the metal-poor stars are plotted in purple. Overlaid in light turquoise are the rest of the Nyx stars, selected as having probabilities >0.75 of belonging to the Nyx velocity Gaussian distribution (Necib et al. 2020b; see Section 2 for more details of the selection of the stars). These stars have been subsampled by a factor of five for clarity of the figure. The metal-poor stars (purple) are coherent with the rest of the sample.

elements of nearby dwarf galaxies (0.5–0.8; Shetrone et al. 2001, 2003). A few metal-rich Nyx giants have [La/Y] $\gtrsim$ 0.5. Unlike the Sgr stars, this is due to their low Y abundance, not high La abundance.

We measured Eu in five Nyx stars observed with MIKE. See Appendix for more details.

4.2. Metal-poor Tail

We first discuss the metal-poor stars of the Bensby sample, against which we compare the abundances of the Nyx stars. The average [Fe/H] of thick-disk stars from Bensby et al. (2014) is likely biased because the selection function for the thick disk used by Bensby et al. (2014) was complex and could not be used to reliably determine the metallicity distribution.

The most metal-poor stars in the Bensby sample have $-1.8 \leqslant$ [Fe/H] ~ -1. The probabilities that these stars belong to the thick disk relative to the halo (see the definition of the ratio of the thick disk to the halo in Section 2) is between TD/H $\sim$ 15 and TD/H $\sim$ 1800, which means that they are probably not halo stars that contaminate the sample.

The Nyx stream has a metal-poor tail that consists of five stars with [Fe/H]~ -2.0 (compared to the average thick-disk star from Bensby et al. (2014) with [Fe/H]~ -0.4). Although this subset has a small sample size, they are clearly isolated in metallicity from the metal-rich majority of the Nyx stars. More specifically, the average metallicity of the metal-poor Nyx stars is $-2.19^{+0.47}_{-0.07}$, compared to $-0.56^{+0.22}_{-0.25}$ of the metal-rich Nyx stars, where the lower and upper limits are the 16th and 84th percentiles, respectively.

The differential abundances of Nyx stars in the metal-poor tail are derived with respect to the similarly metal-poor reference star HIP7162. Figure 3 shows that the differential abundances of the five most metal-poor stars are broadly similar to (within 0.2 dex of) those of the more metal-poor outliers in the Bensby thick-disk stars (Bensby et al. 2014); we recommend caution about this comparison, however, given that the Bensby sample does not extend to the most metal-poor tail of Nyx. The differential abundances of the metal-poor Nyx stars generally have larger uncertainties ($\sigma \sim 0.2$) than the metal-rich ones. These uncertainties are dominated by systematic effects because the differential abundances of metal-poor stars are more susceptible to uncertainties in the stellar parameters (mainly $T_{\rm eff}$ and $\log g$). The Na abundances of the metal-poor Nyx stars are slightly higher than those of the most metal-poor stars of the Bensby sample, by 0.2 dex on average. The α-element abundances of the metal-poor Nyx stars are within 0.2 dex of those of the thick disk.

Figure 3 demonstrates that one of the metal-poor stars (Nyx175906) has a relatively high ratio of [Ba/Y]. Unlike the high [Ba/Y] characteristic of stars in dwarf galaxies, this stems from high [Ba/Fe] abundances, rather than low [Y/Fe] abundances, and is not considered indicative of a low-mass dwarf galaxy origin.

5. Kinematics of Nyx Stars

The Nyx stream has peculiar kinematics for disk stars, with a slow prograde velocity of $\langle v_\phi \rangle = 130$ km s^{-1}, compared to the thick disk at $\langle v_\phi \rangle \sim 200$ km s^{-1} (Gaia Collaboration et al. 2018b), and a large radial velocity component of $\langle v_r \rangle = 134$ km s^{-1} (Necib et al. 2020b), compared to the thick disk at $\langle v_r \rangle \sim 1$ km s^{-1} (Gaia Collaboration et al. 2021; Vieira et al. 2022). Figure 3 shows that while the majority of the Nyx stars has similar chemical abundances to the thick disk, five stars populate a metal-poor tail that could be part of a different component. We now reexamine the Nyx star kinematics to determine whether these metal-poor stars are also kinematically distinct.

Our kinematic quantities for Nyx (including the unobserved sample) and the Bensby et al. (2014) thick-disk stars are determined from Gaia eDR3 (Gaia Collaboration et al. 2021)[22] with radial velocities from Gaia DR2 (Gaia Collaboration et al. 2018a). Velocities in Cartesian coordinates are based on the catalog by Marchetti (2021).[23] We use `Galpy`[24] (Bovy 2015) to derive the eccentricity e, maximum vertical distance $z_{\rm max}$, and apocenter of the stellar orbits, assuming the `MWPotential2014`potential and integrating each orbit backward 1 Gyr

[11] We have checked that the absolute speed distribution ($\|v_r, v_\phi, v_\theta\|$) from Gaia DR3 (Gaia Collaboration et al. 2023) is within 5% of that from Gaia eDR3.
[12] https://sites.google.com/view/tmarchetti/research
[13] http://github.com/jobovy/galpy

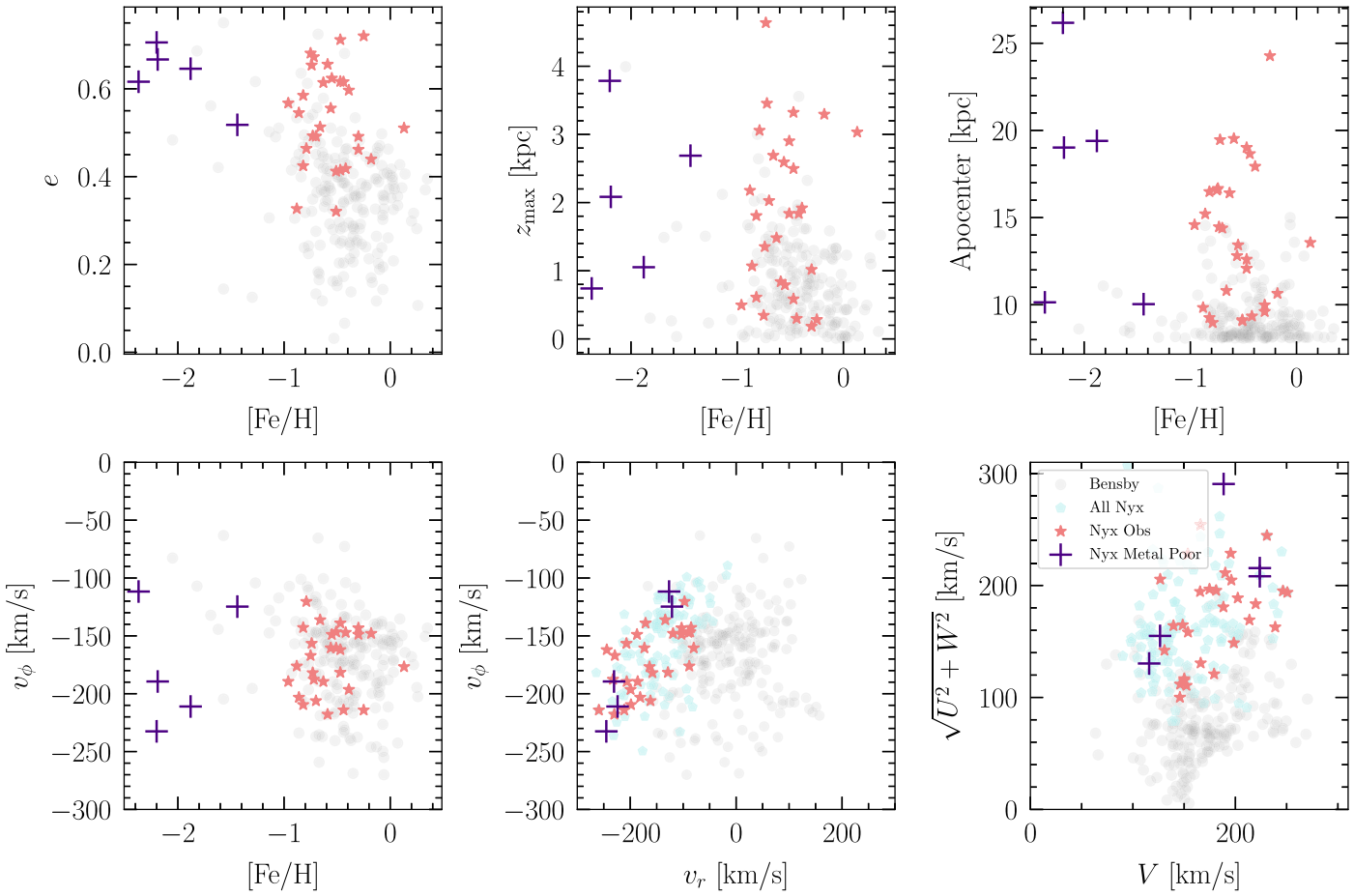

Figure 5. Orbital parameters including eccentricities e, maximum vertical distances from the Galactic plane z_{max}, apocenters, and v_ϕ vs. metallicities [Fe/H] of the Nyx stars, as well as a kinematics plot $v_r - v_\phi$ in galactocentric spherical coordinates, and a Toomre plot of the Nyx stars. The Bensby thick-disk stars are denoted by the light gray circles in the background. The rest of the unobserved sample of Nyx stars is shown in cyan (see Figure 4 for details of the selection of the Nyx stars). These stars are not shown in the orbital parameter panels because we do not have matching metallicity measurements.

in steps of 1 Myr.[25] Figure 4 shows the positions of Nyx stars studied in this paper in galactocentric Cartesian coordinates; the metal-rich stars are indicated in peach, and the five metal-poor stars are highlighted in purple. The velocities of the stars are shown as arrows. The blue background arrows show the kinematics of the rest of the Nyx stars identified by Necib et al. (2020b) with neural network scores $S > 0.95$ (i.e., the confidence that the neural network has in labeling the star as accreted) and high (>0.75) probabilities of belonging to the Nyx best-fit velocity distribution. We find that the direction of the observed metal-poor stars are mostly coherent with the rest of the unobserved Nyx stars, where all the stars display the signature prograde behavior of Nyx kinematics. There is no obvious distinction based on metallicity in the spatial distribution of the stars.

Figure 5 shows the derived orbital parameters of the Nyx and thick-disk stars. The metal-poor stars are highlighted in purple. The top panels of Figure 5 show the derived orbital parameters from `Galpy`. The bottom left panel shows the rotational velocity v_ϕ as a function of the metallicity. The bottom middle panel shows the galactocentric spherical velocities of the observed Nyx stars (peach stars), the metal-poor stars (purple crosses), and the rest of the Nyx stars (cyan pentagons) compared to the reference stars from Bensby et al. (2014; gray circles) in $v_r - v_\phi$ space, while the bottom right panel shows the Toomre diagram of the same stars. Note that the values of v_r and v_ϕ have the opposite sign from Necib et al. (2020b).

As shown in Figure 5, we find systematic differences between the orbital parameters of the Nyx stars and the thick-disk stars. On average,[26] the eccentricities of the thick-disk stars are lower than those of the Nyx stars; the average thick-disk eccentricity is ∼0.4, while that of all the observed Nyx stars[27] is $0.56^{+0.10}_{-0.13}$, and that of only the five metal-poor Nyx stars is $0.65^{+0.04}_{-0.06}$. Note that Bensby et al. (2014) have a complex selection function, but their eccentricity distribution is similar to those found in more representative surveys (e.g., Yan et al. 2019). The maximum vertical distance of these orbits is 0.7 kpc on average for the thick-disk stars, while it is higher for the Nyx stars: $1.84^{+1.21}_{-1.25}$ kpc for the entire Nyx sample and $2.08^{+1.00}_{-1.14}$ kpc for the metal-poor subset. In the top right panel of Figure 5, we find that the apocenters of the thick-disk stars are smaller than those of Nyx stars: ∼9 kpc for the thick disk, compared to the higher values of $14.0^{+5.0}_{-4.3}$ kpc and $19.1^{+2.8}_{-8.9}$ kpc for the observed Nyx sample and the metal-poor subset, respectively.

[14] We adopt a right-handed coordinate system in this analysis.

[15] We avoid a detailed quantitative comparison with the Bensby sample as the latter might not reflect the full distribution of the thick disk. We therefore only quote the mean values of the Bensby distributions.

[16] The numbers quoted are the median and the 16th and 84th percentiles.

In the bottom left panel of Figure 5, we show the distribution of rotational velocity as a function of metallicity of the Nyx and Bensby stars. We find that the metal-rich Nyx stars are consistent with the Bensby stars. However, the five metal-poor stars are split into three stars with a high rotational velocity of $\sim$200 km/s and two stars with a much lower rotational velocity of $\sim$120 km/s, which is further discussed in Section 6.

In the bottom middle panel of Figure 5, we find that the five metal-poor stars are not clustered in exactly the same region of velocity space, but are rather at the edges of the distribution, where three of the stars are on the most radial orbits, while the other two stars are two of the most slowly rotating stars out of the observed Nyx sample. The overall kinematics of the Nyx stars, shown in the Toomre plot in the right bottom panel of Figure 5, are mostly inconsistent with those of thick-disk stars, especially the metal-poor tail. The thick-disk stars tend to have lower $\sqrt{U^2 + W^2}$ values than the Nyx stars, which is consistent with the high radial velocity of the Nyx stars.

To address the discrepancies between the Bensby and Nyx samples, one has to take into account the selection effects of both samples. First, we estimate low contamination rates in the Nyx sample formed in situ based on the neural network classification (Ostdiek et al. 2020), which are expected to be close to zero. However, this estimate could be artificially low due to the bias in the simulations that were used to train the neural network, and it is rather a reflection of the simulation's galactic formation. Second, the Bensby sample has a complex selection function and a 3.0% halo contamination rate; Bensby et al. (2014) provided probability ratios that reflect the likelihood of belonging to the halo compared to the thick disk. These probabilities are based purely on kinematics and therefore assume the distributions of the thick disk, which could include some structure such as Nyx, albeit probably as a small fraction. It is therefore important to keep these systematic differences in mind during this comparative study.

6. Discussion: On the Origin of Nyx

The main result of this paper is that most Nyx stars are metal rich ([Fe/H] > -1) and have detailed chemical compositions similar to the thick disk. The chemical similarity to the thick disk, and in particular, the lack of chemical signatures indicating relative inefficient star formation expected in dwarf galaxies (low-α and high [Ba/Y] or [La/Y]; Venn et al. 2004), clearly shows that Nyx is not composed of one relatively massive and metal-rich dwarf galaxy. A high-α dwarf galaxy would have had to be accreted very early into the Milky Way. The two most significant early mergers into the Milky Way are GSE (Belokurov et al. 2018; Helmi et al. 2018) and the inner galaxy structure Kraken/Heracles (Kruijssen et al. 2020; Horta et al. 2020). These systems have [Fe/H]< -1, while Nyx has an average metallicity [Fe/H]~ -0.5, and thus, if it were a dwarf galaxy, it would be substantially more massive than GSE and Kraken/Heracles. We thus disfavor the scenario in which Nyx is a single massive accretion, agreeing with recent work by other authors who used chemical abundances from large spectroscopic surveys (Zucker et al. 2021; Horta et al. 2023), although we have added additional information from neutron-capture elements. Nyx thus might not be able to make a significant contribution to the dark matter local phase-space distribution: either this stream is due to some baryonic process, or it is from mergers that are too low mass to deposit a large amount of dark matter (e.g., Read et al. 2008; Pillepich et al. 2014); although the latter scenario requires further investigation because it depends on the properties of the mergers, including their orbital parameters, for example.

However, it still remains unclear how a stream like Nyx might be explained, especially given that it has a significant metal-poor component and spans $-2.5 \lesssim$ [Fe/H] $\lesssim -0.5$. We thus briefly consider other possible origins for Nyx. The key observations to explain are (1) the prograde orbit within the thick-disk volume, (2) the relatively high eccentricity of the Nyx stars ($0.4 < e < 0.8$), (3) the chemical similarity between Nyx and the thick disk, and (4) the presence of a metal-poor Nyx population. We note that many of the scenarios discussed below are similar to formation scenarios of the thick disk (whose origin is also still debated), but we consider them here in the context of needing to explain a high-eccentricity subset of the disk.

6.1. Major Mergers

We have shown that the stars in Nyx itself cannot be from a large accretion event, but a large accretion event could still have impacted an existing disk in such a way as to produce the eccentric Nyx stars. There are two main ways in which this could occur. First, a massive merger could dynamically perturb disk stars from circular orbits to hotter orbits and higher eccentricities (e.g., Villalobos & Helmi 2008). The subdominant metal-poor stars originating from the dwarf galaxy could explain the metal-poor Nyx component, and the thick disk would have a range of eccentricities at similar composition that could explain the metal-rich Nyx component. Sales et al. (2009) pointed out that the average eccentricity of the perturbed thick-disk stars would only be $e \sim 0.2$, which disfavors this explanation for Nyx, although additional simulations could be useful. Chemically, it appears that Nyx could be a part of the in situ halo (e.g., Bonaca et al. 2017; Haywood et al. 2018), a high-eccentricity extension of the high-α disk population that may have originated from a dynamically heated disk (e.g., Naidu et al. 2020). The metal-poor Nyx stars could be a part of the metal-poor tail of the distribution. The broad, continuous eccentricity distribution of the in situ halo could explain the high eccentricity of Nyx stars. However, we do not consider the evidence conclusive because it remains unclear why an additional overdensity in the kinematic space for Nyx should overlap with the normal location of the in situ halo.

Alternatively, a massive gas-rich merger might have caused Nyx. It has been proposed that the thick disk could be formed during a turbulent epoch of gas-rich mergers prior to the formation of the thin disk (Brook et al. 2004). This is an attractive explanation because it could explain both the metal-rich and metal-poor stars in Nyx: the predominantly metal-rich Nyx stars would have formed in the Milky Way using gas stripped from accreted satellites, while the subdominant metal-poor Nyx stars would come from the accreted galaxy.[28] However, because gas is collisional, it would end up in orbits distinct from those of the accreted stars. Sales et al. (2009) found in simulations that the stars formed from the stripped gas would only have $e \sim 0.2$, which is too low to explain the behavior of the metal-rich Nyx stars. Therefore, we find it unlikely that the Nyx stars originated from a major merger event, whether through the dynamical heating scenario or the gas-rich merger scenario.

[17] Also see recent work (e.g., Santistevan et al. 2021; Sestito et al. 2021).

6.2. Minor Mergers

Abadi et al. (2003) proposed that over 60% of the Galactic thick disk could be stars accreted from multiple tidally disrupted satellite galaxies on prograde orbits (also found in more recent simulations; see Mardini et al. 2022). Sales et al. (2009) showed that this scenario would result in relatively high eccentricities, $e \sim 0.5$, consistent with most observed Nyx stars. A minor merger could provide the metal-poor Nyx stars and might have produced the metal-rich ones by pulling a small fraction of disk stars into the same orbit.

The high-α abundances of the metal-poor Nyx stars challenge this idea: most lower-mass dwarf galaxies have low-α for their most metal-rich ([Fe/H] ~ -1.0) stars (Venn et al. 2004) because maintaining high-α requires a high star formation efficiency that keeps the ratio of core-collapse to Type Ia supernova high. However, high-α can be maintained if the minor merger occurred relatively early. Indeed, two candidate accretion events have high-α: the inner galaxy structure Kraken/Koala/Heracles (Forbes 2020; Horta et al. 2020; Kruijssen et al. 2020), and the Atari disk (or metal-weak thick disk; e.g., Norris et al. 1985; Chiba & Beers 2000; Carollo et al. 2019; An & Beers 2020; Mardini et al. 2022). Neither of these known events is the same as Nyx: Kraken is restricted to galactocentric radii $r < 5$ kpc, while Atari has a much lower mean radial velocity ($\langle v_r \rangle \sim 10$ km s^{-1}). We thus consider an early minor merger to be a plausible explanation for Nyx. Note that a lower-mass merger could still result in a dark matter substructure, but would likely make a fairly negligible (<10%) contribution to the local phase-space distribution (Pillepich et al. 2014).

6.3. Radial Migration

Resonant scattering of spiral arms may cause disk stars on near-circular orbits to move radially, while preserving their eccentricities (e.g., Sellwood & Binney 2002; Roš et al. 2008). Based on radial migration, Schönrich & Binney (2009) constructed chemical evolution models of the Milky Way that demonstrate the coevolution of the Galactic thick and thin disk. They found that the resulting [α/Fe] versus [Fe/H] trend closely resembled that from Venn et al. (2004), and displayed a dichotomy between the thick and thin disks. Ruchti et al. (2011) investigated the chemodynamics of the high-α metal-poor thick-disk stars ($-2.5 \lesssim$ [Fe/H] $\lesssim -0.7$) from RAVE (Steinmetz et al. 2006) and considered radial migration as one of the possible origins of these stars. Thus, radial migration might be able to produce a predominantly metal-rich stellar population that is chemically similar to the thick disk and a subdominant high-α metal-poor stellar population. However, radial migration generally results in only moderate eccentricities of $e \sim 0.2$ (as well as in an eccentricity cutoff at $e \sim 0.6$; Sales et al. 2009), while those of the Nyx stars are $0.56^{+0.10}_{-0.13}$.

6.4. Relic of Thick-disk Formation

Several recent studies have attempted to study the metal-poor in situ component of the Milky Way with spectroscopic surveys (Xiang & Rix 2022; Belokurov & Kravtsov 2022; Conroy et al. 2022). These studies have broadly concluded that between $-2.5 \lesssim$ [Fe/H] $\lesssim -0.5$ (corresponding to an age ~13 Gyr ago), the Milky Way both rapidly spun up (from $\langle v_\phi \rangle < 100$ km s^{-1} up to $\langle v_\phi \rangle \sim 175$ km s^{-1}) and greatly increased its star formation efficiency before merging with GSE. In this early turbulent gas-rich disk, it is plausible that a subset of in situ disk stars could form with high eccentricities (e.g., van Donkelaar et al. 2022).

Nyx could potentially be a remnant of this early time in either a distinct phase of formation or in a high-eccentricity tail of the overall thick-disk formation. Indeed, the Nyx stars span the range of rotational velocities (bottom left panel of Figure 5) and metallicities expected for this scenario. A challenge for this scenario is that on average, the azimuthal velocities are expected to increase with metallicity (see, e.g., Belokurov & Kravtsov 2022), while in Nyx, many of the fastest-rotating stars are the most metal-poor stars (Figure 5). Still, given the uncertainties in the details of early Milky Way formation, we consider this a promising explanation. An obvious conclusion of this scenario is that structures such as Nyx should be present at any position within the disk, not just in the solar neighborhood.

7. Conclusions

We analyzed the chemical abundances and kinematics of 34 Nyx stars observed with Magellan/MIKE or Keck/HIRES. These high-purity stars were selected from 94 Nyx stars in the accreted star catalog defined by Necib et al. (2020b). In order to determine the origin of the Nyx stars, we provided a detailed chemodynamic comparison of these Nyx stars to the thick-disk stars from Bensby et al. (2014). We employed a differential abundance analysis to study the chemical compositions of the Nyx stars.

Our analysis reveals that the chemical abundances of the Nyx stars are mostly consistent with the high-α thick-disk stars, with the exception of five stars in the metal-poor tail ([Fe/H] ~ -2.0). The abundance results we attain have a much higher precision than those from RAVE-on (Casey et al. 2017), which was used in the Nyx discovery paper (Necib et al. 2020b), and they show that the metal-rich Nyx stars are chemically consistent with thick-disk stars. Both metal-poor and metal-rich Nyx stars have overall similar kinematic properties, although the metal-poor Nyx stars have somewhat higher eccentricities ($0.5 < e < 0.7$) than the metal-rich Nyx stars ($e \sim 0.5$).

The chemical abundances clearly rule out Nyx as the result of a single massive dwarf galaxy merger. However, it is still not known how a population of stars can be produced whose chemistry is identical to that of the thick disk, but that have these high eccentricities. We consider multiple formation scenarios, finding that the most likely scenarios are that Nyx is the signature of an early minor merger or that Nyx is an unusual phase in the Milky Way's thick-disk formation history. The former scenario—Nyx originated from multiple small dwarf galaxy mergers—would require that the merger event occurred relatively early, and it would likely only make a fairly negligible (<10%) contribution to the dark matter local phase-space distribution; whereas the latter scenario—Nyx is the relic of the early thick-disk formation history—might be challenged by the fact that the fastest-rotating Nyx stars are the most metal-poor ones. The latter scenario clearly suggests that structures similar to Nyx should exist elsewhere within the disk.

Future simulations and observations might shed light on the possible formation scenario of the Nyx stream. Specifically, isolated simulations of early accretion events between the

Milky Way's primordial disk and multiple satellite dwarf galaxies could explore the formation history of the Galactic thick disk. Recent advances, particularly in simulations of stable disk formation and disk perturbations, open the path to future studies of Nyx-like structures and their origins (e.g., Ejdetjärn et al. 2022). A detailed chemodynamic study of the stars produced in such streams would help determine whether the metal-rich Nyx stars and the high-eccentricity metal-poor tail formed through multiple minor dwarf galaxy mergers. If simulations can produce stars with high-α abundances from early mergers, it could provide evidence for this scenario.

Alternatively, if Nyx is a remnant of the early turbulent Milky Way formation, future Gaia data releases and spectroscopic surveys such as SDSS-V, WEAVE, and 4MOST (Dalton et al. 2012; de Jong et al. 2016; Kollmeier et al. 2017) should identify similar structures farther away from the solar neighborhood. A combination of high-resolution simulations with current and future observations should thus aid in piecing together the origin of Nyx and understanding its role in the formation and structure of our Galaxy.

Acknowledgments

We are grateful to E. Holmbeck and R. Naidu for their contributions to the observation of Nyx stars. We thank the referee for comments that significantly improved this paper. S. W. thanks R. Naidu, P. Re Fiorentin, and A. Wetzel for helpful discussions. L.N. and M.L. thank T. Cohen and B. Ostdeik for their early collaboration and the Nyx discovery.

A.P.J. acknowledges support from NSF grant AST 2206264. M.L. is supported by the DOE under Award Number DE-SC0007968. M.A.C.dl R. is supported by a Stanford Science Fellowship.

This work presents results from the European Space Agency (ESA) space mission Gaia. Gaia data are being processed by the Gaia Data Processing and Analysis Consortium (DPAC). Funding for the DPAC is provided by national institutions, in particular the institutions participating in the Gaia MultiLateral Agreement (MLA). The Gaia mission website is https://www.cosmos.esa.int/gaia. The Gaia archive website is https://archives.esac.esa.int/gaia. This research makes use of public auxiliary data provided by ESA/Gaia/DPAC/CU5 and prepared by Carine Babusiaux.

This research has made use of the NASA/IPAC Infrared Science Archive, which is funded by the National Aeronautics and Space Administration and operated by the California Institute of Technology.

This research has made use of the Keck Observatory Archive (KOA), which is operated by the W. M. Keck Observatory and the NASA Exoplanet Science Institute (NExScI), under contract with the National Aeronautics and Space Administration. This paper includes data gathered with the 6.5 m Magellan Telescopes located at Las Campanas Observatory, Chile.

Facilities: Keck (HIRES), Magellan (MIKE), Gaia.

Software: `CarPy` (Kelson 2003), `smhr` (Casey 2014; Ji et al. 2020b), `numpy` (Harris et al. 2020), `scipy` (Virtanen et al. 2020), `matplotlib` (Hunter 2007), `astropy` (Astropy Collaboration et al. 2013, 2018), `AGAMA` (Vasiliev 2019).

Appendix
Absolute Abundances and Uncertainties

We determine the absolute chemical abundances of the observed Nyx stars—i.e., assuming that we have accurate atomic data, model atmospheres, and radiative transfer physics. The uncertainties of the absolute abundances are determined following Ji et al. (2020b), i.e., propagating spectrum noise and stellar parameter uncertainties into the final results with a weighted average, where the weights generalize the usual inverse-variance weight under the assumption that individual line abundances are correlated due to stellar parameters. There exist significant zeropoint offsets ($\delta \sim 0.2$) between the absolute abundances of the Nyx stars and the literature (see, e.g., Bensby et al. 2014).

Here, we discuss the absolute abundances of Al I, K I, Sc II, V I, Mn I, and Eu II. The Al and K abundances are determined using equivalent width measurement, while the Sc II, V I, Mn I, and Eu II abundances are determined using spectral synthesis. These abundances are not determined differentially for the following reasons: all Al lines and the Eu line at 6645 fall into chip gaps for the Nyx stars observed with Keck/HIRES, and are only measured in the six stars observed with Magellan/MIKE;[29] and the K, Sc, V, and Mn abundances were not determined by Bensby et al. (2014).

Figure 6 shows the absolute abundances of the Nyx stars for these six elements, color-coded by effective temperatures. The abundances of 3 Sagittarius (Sgr) dwarf galaxy stars from McWilliam et al. (2013) and 12 Sgr giant stars from Sbordone et al. (2007) are also shown for comparison.

As shown in Figure 6, the odd-Z (Al, Sc, and V) abundances of Sgr stars are significantly lower (by $\sim$0.6 dex) than those of the metal-rich Nyx stars, although their metallicities are slightly higher. The iron-peak (Mn) abundances have a relatively small dispersion ($\sim$0.1 dex). [Mn/Fe] displays a slightly upward trend with respect to [Fe/H]. Figure 6 also shows the [Ba/Eu] ratios of the Nyx stars, an indicator of the relative amount of *s*-process and *r*-process enrichment. The [Ba/Eu] ratios increase with metallicity from a pure *r*-process ratio of [Ba/Eu] $= -0.8$ (Sneden et al. 2008) to a fairly *s*-process-dominated ratio [Ba/Eu] $\gtrsim 0.0$, following the rise in the *s*-process (Simmerer et al. 2004). One of the five Nyx stars in the metal-poor tail (Nyx122147) has a detectable Eu abundance of [Ba/Fe] $= 0.572$ and [Ba/Eu] $= -0.515$, indicating *r*-process domination with some *s*-process influence. In Figure 6, the overall [Eu/Fe] versus [Fe/H] trend is flat, matching the Milky Way at these metallicities (Battistini & Bensby 2016) ([Eu/Fe] $\sim$ 0.3). There are too few Eu measurements to robustly measure the expected *r*-process scatter.

ORCID iDs

Shuyu Wang (汪书玉) https://orcid.org/0000-0001-6663-5605
Lina Necib https://orcid.org/0000-0003-2806-1414
Alexander P. Ji https://orcid.org/0000-0002-4863-8842
Xiaowei Ou https://orcid.org/0000-0002-4669-9967
Mariangela Lisanti https://orcid.org/0000-0002-8495-8659
Mithi A. C. de los Reyes https://orcid.org/0000-0002-4739-046X
Allison L. Strom https://orcid.org/0000-0001-6369-1636

[18] Although bluer Eu lines are visible at 4129 and 4205 Å, these wavelength regions are too strongly blended for accurate abundance analysis.

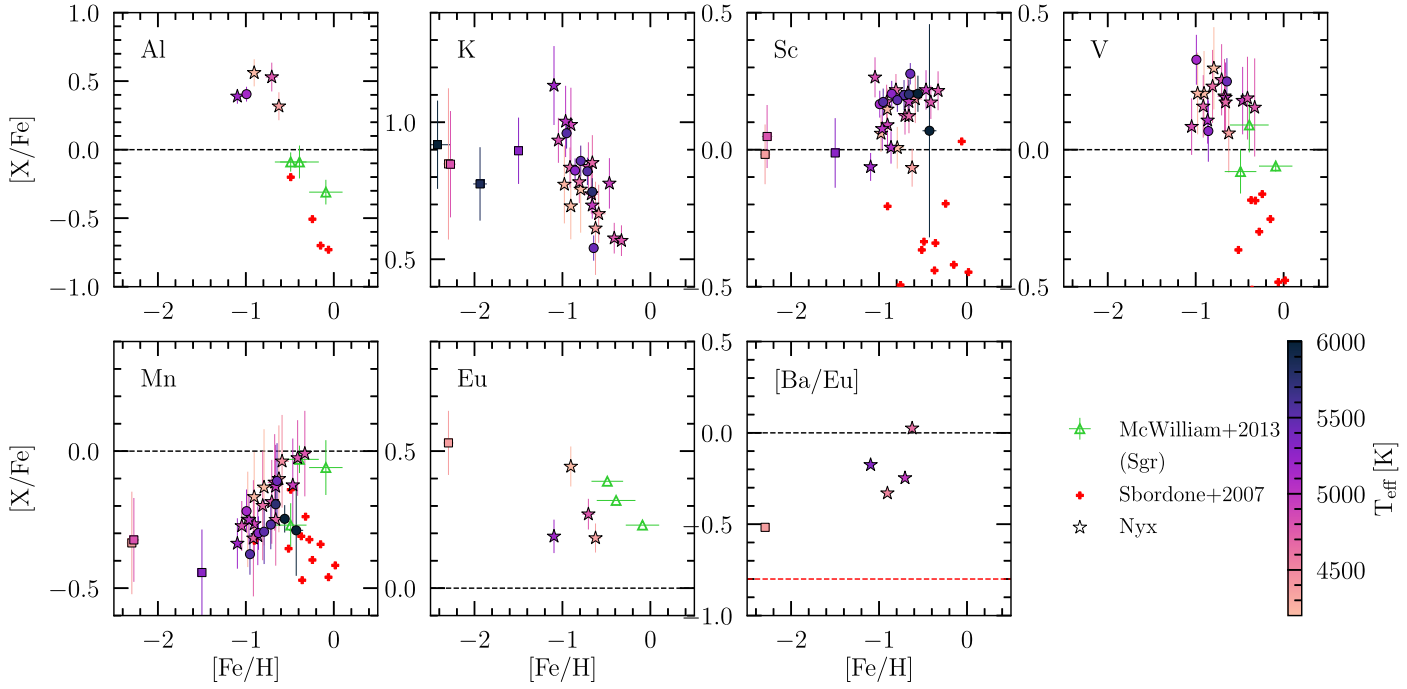

Figure 6. Absolute chemical abundances ([X/Fe] vs. [Fe/H]. The *y*-axis is [X/Fe], except in the panel where another ratio is indicated) of the observed Nyx stars, color-coded by effective temperature, $T_{\rm eff}$. The effective temperatures range from 4200 to 6000 K. For comparison, 3 Sgr dwarf galaxy stars from McWilliam et al. (2013) are shown by green triangles. The 12 Sgr dwarf galaxy giants from Sbordone et al. (2007) are indicated by red plusses. The dashed line at [X/Fe] = 0.0 is shown in each panel as a reference. The dashed red line at [Ba/Eu] = −0.8 indicates the pure *r*-process ratio (Sneden et al. 2008). In general, the chemical abundances of the metal-rich Nyx component are distinct from those of the Sgr stars.

Mimi Truong https://orcid.org/0000-0001-9812-4957

References

Abadi, M. G., Navarro, J. F., Steinmetz, M., & Eke, V. R. 2003, ApJ, 597, 21
Abdurro'uf, Accetta, K., Aerts, C., et al. 2022, ApJS, 259, 35
Ahumada, R., Prieto, C. A., Almeida, A., et al. 2020, ApJS, 249, 3
An, D., & Beers, T. C. 2020, ApJ, 897, 39
Asplund, M., Grevesse, N., Sauval, A. J., & Scott, P. 2009, ARA&A, 47, 481
Astropy Collaboration, Price-Whelan, A. M., Sipőcz, B. M., et al. 2018, AJ, 156, 123
Astropy Collaboration, Robitaille, T. P., Tollerud, E. J., et al. 2013, A&A, 558, A33
Battistini, C., & Bensby, T. 2016, A&A, 586, A49
Belokurov, V., Erkal, D., Evans, N. W., Koposov, S. E., & Deason, A. J. 2018, MNRAS, 478, 611
Belokurov, V., & Kravtsov, A. 2022, MNRAS, 514, 689
Bengio, Y. 2012, in Proc. of ICML Workshop on Unsupervised and Transfer Learning, ed. I. Guyon et al. (Bellevue, WA: PMLR), 17
Bensby, T., Feltzing, S., & Lundström, I. 2003, A&A, 410, 527
Bensby, T., Feltzing, S., Lundström, I., & Ilyin, I. 2005, A&A, 433, 185
Bensby, T., Feltzing, S., & Oey, M. S. 2014, A&A, 562, A71
Bernstein, R., Shectman, S. A., Gunnels, S. M., Mochnacki, S., & Athey, A. E. 2003, Proc. SPIE, 4841, 1694
Bonaca, A., Conroy, C., Wetzel, A., Hopkins, P. F., & Kereš, D. 2017, ApJ, 845, 101
Bovy, J. 2015, ApJS, 216, 29
Brook, C. B., Kawata, D., Gibson, B. K., & Freeman, K. C. 2004, ApJ, 612, 894
Bruch, T., Read, J., Baudis, L., & Lake, G. 2009, ApJ, 696, 920
Buder, S., Sharma, S., Kos, J., et al. 2021, MNRAS, 506, 150
Bullock, J. S., & Johnston, K. V. 2005, ApJ, 635, 931
Carollo, D., Chiba, M., Ishigaki, M., et al. 2019, ApJ, 887, 22
Caruana, R. 1994, in NIPS: Proc. of the 7th International Conference on Neural Information Processing Systems, 7, ed. G. Tesauro, D. Touretzky, & T. Leen (Cambridge, MA: MIT Press), 657
Casey, A. R. 2014, PhD thesis, Australian National Univ., Canberra doi:10.5281/ZENODO.49493
Casey, A. R., Hawkins, K., Hogg, D. W., et al. 2017, ApJ, 840, 59
Castelli, F., & Kurucz, R. L. 2003, in IAU Symp. 210, Modelling of Stellar Atmospheres, ed. N. Piskunov, W. W. Weiss, & D. F. Gray (San Francisco, CA: ASP), A20
Chiba, M., & Beers, T. C. 2000, AJ, 119, 2843
Choi, J., Dotter, A., Conroy, C., et al. 2016, ApJ, 823, 102
Conroy, C., Weinberg, D. H., Naidu, R. P., et al. 2022, arXiv:2204.02989
Cseh, B., Világos, B., Roriz, M. P., et al. 2022, A&A, 660, A128
Dalton, G., Trager, S. C., Abrams, D. C., et al. 2012, Proc. SPIE, 8446, 84460P
de Jong, R. S., Barden, S. C., Bellido-Tirado, O., et al. 2016, Proc. SPIE, 9908, 99081O
Donlon, T., Newberg, H. J., Kim, B., & Lepine, S. 2022, ApJL, 932, L16
Donlon, T., Newberg, H. J., Weiss, J., Amy, P., & Thompson, J. 2019, ApJ, 886, 76
Ejdetjärn, T., Agertz, O., Östlin, G., Renaud, F., & Romeo, A. B. 2022, MNRAS, 514, 480
Fanelli, C., Origlia, L., Oliva, E., et al. 2021, A&A, 645, A19
Font, A. S., Johnston, K. V., Bullock, J. S., & Robertson, B. E. 2006, ApJ, 638, 585
Forbes, D. A. 2020, MNRAS, 493, 847
Forsberg, R., Jönsson, H., Ryde, N., & Matteucci, F. 2019, A&A, 631, A113
Freeman, K., & Bland-Hawthorn, J. 2002, ARA&A, 40, 487
Gaia Collaboration, Brown, A. G. A., Vallenari, A., et al. 2016b, A&A, 595, A2
Gaia Collaboration, Brown, A. G. A., Vallenari, A., et al. 2018a, A&A, 616, A1
Gaia Collaboration, Brown, A. G. A., Vallenari, A., et al. 2021, A&A, 649, A1
Gaia Collaboration, Katz, D., Antoja, T., et al. 2018b, A&A, 616, A11
Gaia Collaboration, Prusti, T., de Bruijne, J. H. J., et al. 2016a, A&A, 595, A1
Gaia Collaboration, Vallenari, A., Brown, A. G. A., et al. 2023, A&A, 674, A1
Gryncewicz, R., Newberg, H. J., Martin, C. T. D., II, & Amy, P. M. 2021, ApJ, 910, 102
Harris, C. R., Millman, K. J., van der Walt, S. J., et al. 2020, Natur, 585, 357
Haywood, M., Matteo, P. D., Lehnert, M. D., et al. 2018, ApJ, 863, 113
Helmi, A. 2008, A&ARv, 15, 145
Helmi, A. 2020, ARA&A, 58, 205
Helmi, A., Babusiaux, C., Koppelman, H. H., et al. 2018, Natur, 563, 85
Helmi, A., & White, S. D. M. 1999, MNRAS, 307, 495
Herzog-Arbeitman, J., Lisanti, M., Madau, P., & Necib, L. 2018a, PhRvL, 120, 041102
Herzog-Arbeitman, J., Lisanti, M., & Necib, L. 2018b, JCAP, 2018, 052

Hinkle, K., Wallace, L., Valenti, J., et al. 2000, Visible and Near Infrared Atlas of the Arcturus Spectrum 3727-9300 A (San Francisco, CA: ASP)
Hopkins, P. F. 2015, MNRAS, 450, 53
Hopkins, P. F., Kereš, D., Oñorbe, J., et al. 2014, MNRAS, 445, 581
Hopkins, P. F., Wetzel, A., Kereš, D., et al. 2018, MNRAS, 480, 800
Horta, D., Schiavon, R. P., Mackereth, J. T., et al. 2020, MNRAS, 500, 1385
Horta, D., Schiavon, R. P., Mackereth, J. T., et al. 2023, MNRAS, 520, 5671
Hunter, J. D. 2007, CSE, 9, 90
IRSA 2022, Galactic Dust Reddening and Extinction, IPAC, doi:10.26131/IRSA537
Ji, A. P., Li, T. S., Hansen, T. T., et al. 2020b, AJ, 160, 181
Ji, A. P., Li, T. S., Simon, J. D., et al. 2020a, ApJ, 889, 27
Johnston, K. V. 1998, ApJ, 495, 297
Jönsson, H., Ryde, N., Nordlander, T., et al. 2017, A&A, 598, A100
Kelson, D. D. 2003, PASP, 115, 688
Kollmeier, J. A., Zasowski, G., Rix, H.-W., et al. 2017, arXiv:1711.03234
Koppelman, H. H., Helmi, A., Massari, D., Price-Whelan, A. M., & Starkenburg, T. K. 2019, A&A, 631, L9
Kruijssen, J. M. D., Pfeffer, J. L., Chevance, M., et al. 2020, MNRAS, 498, 2472
Kunder, A., Kordopatis, G., Steinmetz, M., et al. 2017, ApJ, 153, 75
Ling, F.-S., Nezri, E., Athanassoula, E., & Teyssier, R. 2010, JCAP, 2010, 012
Lomaeva, M., Jönsson, H., Ryde, N., Schultheis, M., & Thorsbro, B. 2019, A&A, 625, A141
Mackereth, J. T., Schiavon, R. P., Pfeffer, J., et al. 2018, MNRAS, 482, 3426
Marchetti, T. 2021, MNRAS, 503, 1374
Mardini, M. K., Frebel, A., Chiti, A., et al. 2022, ApJ, 936, 78
Matsuno, T., Dodd, E., Koppelman, H. H., et al. 2022, A&A, 665, A46
McWilliam, A. 1997, ARA&A, 35, 503
McWilliam, A., Wallerstein, G., & Mottini, M. 2013, ApJ, 778, 149
Monaco, L., Bellazzini, M., Bonifacio, P., et al. 2007, A&A, 464, 201
Mucciarelli, A., Bellazzini, M., & Massari, D. 2021, A&A, 653, A90
Myeong, G. C., Vasiliev, E., Iorio, G., Evans, N. W., & Belokurov, V. 2019, MNRAS, 488, 1235
Naidu, R. P., Conroy, C., Bonaca, A., et al. 2020, ApJ, 901, 48
Necib, L., Ostdiek, B., Lisanti, M., et al. 2020a, ApJ, 903, 25
Necib, L., Ostdiek, B., Lisanti, M., et al. 2020b, NatAs, 4, 1078
Nissen, P. E., & Schuster, W. J. 2010, A&A, 511, L10
Norris, J., Bessell, M. S., & Pickles, A. J. 1985, ApJS, 58, 463
Ostdiek, B., Necib, L., Cohen, T., et al. 2020, A&A, 636, A75
Pillepich, A., Kuhlen, M., Guedes, J., & Madau, P. 2014, ApJ, 784, 161
Purcell, C. W., Bullock, J. S., & Kaplinghat, M. 2009, ApJ, 703, 2275
Read, J. I., Lake, G., Agertz, O., & Debattista, V. P. 2008, MNRAS, 389, 1041
Read, J. I., Mayer, L., Brooks, A. M., Governato, F., & Lake, G. 2009, MNRAS, 397, 44
Robertson, B., Bullock, J. S., Font, A. S., Johnston, K. V., & Hernquist, L. 2005, ApJ, 632, 872
Rodriguez-Gomez, V., Sales, L. V., Genel, S., et al. 2017, MNRAS, 467, 3083
Roederer, I. U., Sakari, C. M., Placco, V. M., et al. 2018, ApJ, 865, 129
Roškar, R., Debattista, V. P., Stinson, G. S., et al. 2008, ApJ, 675, L65
Ruchti, G. R., Fulbright, J. P., Wyse, R. F. G., et al. 2011, ApJ, 737, 9
Sales, L. V., Helmi, A., Abadi, M. G., et al. 2009, MNRAS: Lett., 400, L61
Sanderson, R. E., Wetzel, A., Loebman, S., et al. 2020, ApJS, 246, 6
Santistevan, I. B., Wetzel, A., Sanderson, R. E., et al. 2021, MNRAS, 505, 921
Sbordone, L., Bonifacio, P., Buonanno, R., et al. 2007, A&A, 465, 815
Schlafly, E. F., & Finkbeiner, D. P. 2011, ApJ, 737, 103
Schönrich, R., & Binney, J. 2009, MNRAS, 396, 203
Sellwood, J. A., & Binney, J. J. 2002, MNRAS, 336, 785
Sestito, F., Buck, T., Starkenburg, E., et al. 2021, MNRAS, 500, 3750
Shetrone, M., Venn, K. A., Tolstoy, E., et al. 2003, AJ, 125, 684
Shetrone, M. D., Cote, P., & Sargent, W. L. W. 2001, ApJ, 548, 592
Simmerer, J., Sneden, C., Cowan, J. J., et al. 2004, ApJ, 617, 1091
Sneden, C., Cowan, J. J., & Gallino, R. 2008, ARA&A, 46, 241
Sneden, C. A. 1973, PhD thesis, Univ. Texas, Austin
Sobeck, J. S., Kraft, R. P., Sneden, C., et al. 2011, AJ, 141, 175
Steinmetz, M., Zwitter, T., Siebert, A., et al. 2006, AJ, 132, 1645
van Donkelaar, F., Agertz, O., & Renaud, F. 2022, MNRAS, 512, 3806
Vasiliev, E. 2019, MNRAS, 482, 1525
Venn, K. A., Irwin, M., Shetrone, M. D., et al. 2004, AJ, 128, 1177
Vieira, K., Carraro, G., Korchagin, V., et al. 2022, ApJ, 932, 28
Villalobos, Á., & Helmi, A. 2008, MNRAS, 391, 1806
Virtanen, P., Gommers, R., Oliphant, T. E., et al. 2020, NatMe, 17, 261
Vogt, S. S., Allen, S. L., Bigelow, B. C., et al. 1994, Proc. SPIE, 2198, 362
Wetzel, A. R., Hopkins, P. F., Kim, J.-h., et al. 2016, ApJL, 827, L23
White, S. D. M., & Rees, M. J. 1978, MNRAS, 183, 341
Xiang, M., & Rix, H.-W. 2022, Natur, 603, 599
Yan, Y., Du, C., Liu, S., et al. 2019, ApJ, 880, 36
Yuan, Z., Myeong, G. C., Beers, T. C., et al. 2020, ApJ, 891, 39
Zucker, D. B., Simpson, J. D., Martell, S. L., et al. 2021, ApJL, 912, L30